Gravitational Instability of Thickened yet Compositionally Buoyant Tibetan Mantle Lithosphere

Gregory A. Houseman
School of Geophysics and Information Technology, China Univ. of Geosciences, Beijing, China;
and School of Earth and Environment, University of Leeds, Leeds, LS2 9JT, UK

Philip C. England
Department of Earth Sciences, Oxford University, S Parks Rd, Oxford, OX1 3AN, UK

Lynn A. Evans
School of Earth, Atmosphere and Environment, Monash University, Clayton, VIC, Australia

Abstract

The Tibetan plateau, one of the major topographic features of the Earth, presents many unanswered questions regarding its evolution, present structure, and continuing geological activity. The extensive crustal thickening that is attributed to continental convergence between India and Eurasia sustained for the past 55 Myr, and continuing today, is underlain by an upper mantle in which relatively fast shear-wave speeds are measured to depths of 200 km and more. Although the high elevation of the plateau can be attributed mainly to the thickness of the crust, the observation that the plateau is now extending is evidence that the lithosphere has increased its gravitational potential energy since it was thickened. Extensive volcanism during the current continental collision, additionally implies that the lithosphere and/or uppermost mantle of Tibet was re-heated. Replacement of mantle lithosphere by asthenosphere in a convective thinning process has been advanced as an explanation of that re-heating, but that process has been difficult to reconcile with the high shear-wave velocities measured in the upper mantle beneath the plateau. However, a model based on a restricted overturn of a depleted, metasomatised, mantle lithosphere in the upper 200 km of the mantle can reconcile these apparently contradictory observations. Such overturn can explain how the observed distribution of seismic velocities has been produced, how heat is injected into the lithosphere producing transient uplift, and how mantle-derived melts can rapidly reach the base of the crust in widely distributed locations across the plateau.

Introduction

The crustal thickness of the Tibetan Plateau varies between about 60 and 75 km (Nábelek et al., 2009; Kind and Yuan, 2010; Yuan et al., 1997; Zhang et al., 2011; Gao et al., 2013; Shen et al., 2016), in contrast with normal continental crustal thickness of 35 to 40 km. The Tibetan crust has been thickened by the continuing continental collision of India and Eurasia since at least 55 Ma (Yin and Harrison, 2000; Garzanti, 2008). Thrust faulting, often associated with older suture zones, enabled crustal thickening (Yin and Harrison, 2000). Throughout this period, large-scale lateral displacements have been mediated by a combination of continuous deformation and displacements on strike-slip fault systems (England and Molnar, 2005; Tapponnier and Molnar, 1977; Fang et al., 2024). A combination of strike-slip and thrust deformation continues to govern deformation on the margins of the plateau (Burchfiel et al., 2008; Ou et al., 2022). However, since about 10-15 Ma, the onset of rifting on a set of north-south structures (Armijo et al., 1986; Styron et al., 2013) indicates that most of the plateau has been extending in the E-W direction (Gan et al., 2021) faster than it shortens in the N-S direction. From current geodetic dilatation rates, the crust of the plateau is estimated to have thinned by more than 5 km during this period (Ge et al., 2015). Although some authors, beginning with Argand (1924) have argued for the concept of Tibet being raised by the under-thrusting of a rigid "Greater India" plate that extends 1000 km or more across the plateau, we assume for the purpose of these calculations that the Tibetan lithosphere in general has remained vertically coherent as it has been shortened, thickened and sheared during the India-Asia collision.

England and Houseman (1989) argued that the mechanism which would most simply explain the change in the tectonic environment of the plateau, from convergence and thickening to extension and thinning, involved the removal of relatively dense, colder, mantle lithosphere from beneath the plateau, and its replacement by hot asthenosphere. They suggested, following Houseman et al. (1981), that this could be accomplished simply by a convective destabilisation of the viscous upper mantle. In mechanical terms, heating or replacement of relatively cold lithosphere causes an elevation increase under isostasy, so that the vertical compressive stress component can increase to the point where it is greater than one of the principal horizontal compressive stress components. The re-orientation of the principal stresses can then cause east-west extension rates to exceed north-south shortening rates, allowing the onset of normal faulting alongside persistent strike-slip shear. The arguments in favour of a convective thinning event beneath Tibet at around 10-15 Ma seemed robust until studies based on the propagation of seismic surface waves showed that a layer of cold, relatively fast, mantle remains in place beneath much of the Tibetan Plateau at depths of around 200 km (Huang et al., 2003; Priestley et al., 2006).

A simplified tectonic map of the Tibetan Plateau (Fig. 1) shows the major suture zones separating Lhasa, Qiangtang and Songpan-Ganze terranes progressively coalesced by pre-collision ocean closure, and subsequently shortened by North-South convergence (Yin and Harrison, 2000). Fig. 1 also shows locations of normal faults delineating rifts developed in the south of the plateau as a consequence of East-West extension dating from the mid-Miocene. An important indication of the process that changed the tectonic environment of Tibet follows from the widespread post-collision volcanism affecting most parts of the Tibetan Plateau (Fig. 1; Chung et al., 2005; Ding et al., 2003). In particular, potassic to ultrapotassic volcanic rocks in the Qiangtang terrane (~45-29 Ma), the central and western Lhasa terrane (~25-8 Ma) and the Songpan-Ganzi terrane (~17-1 Ma) are interpreted to have been derived from metasomatised mantle sources which may have undergone distinct and complex enrichment histories (Chung et al., 2005; Ding et al., 2003). The relatively high potassium content of these magmas indicates a K-rich phase like phlogopite in the source region, interpreted as representing enriched sub-continental mantle lithosphere. The age of the enrichment is debated, with Ding et al. (2003) suggesting that it could be attributed to different phases of Mesozoic and Cenozoic subduction on the major suture zones that separate Lhasa, Qiangtang and Songpan-Ganzi terranes, whereas Turner et al. (1996) inferred Proterozoic or even Archaean age for the metasomatism based on radiogenic isotope ratios. In general the potassic lavas are associated with late Cenozoic rift systems that are diagnostic of the onset of east-west extension in the plateau, and the spatial and temporal correlations imply that the potassic magmatism and the lithospheric extension are symptoms of the same process. Based on thermal arguments, Turner et al. (1993) concluded that the only plausible means to attain temperatures high enough for melting within the lithospheric mantle beneath Tibet was a widespread convective thinning event affecting most of Tibet. Chung et al. (2005) interpreted distinct thinning events affecting the lithosphere under the different terranes. Consistent with the idea of multiple events, Ding et al. (2003) pointed out that melting related to subduction at the thrust systems on the terrane boundaries seemed to explain why magmatic belts with distinctive source signatures are aligned with the major terrane boundaries.

Whether the mantle lithosphere beneath Tibet has been thinned or not is thus a central question in the interpretation of both tectonic and magmatic evolution of the Tibetan lithosphere. Measurement of shear velocity versus depth obtained from tomographic analysis of surface waves provides a key constraint on the question. Priestley et al. (2006) used this method to map the base of the East Asian lithosphere, concluding that the Tibetan lithosphere remains in place, and in fact that the lithosphere beneath Tibet is similar to tectonically stable Archaean and Proterozoic cratons which may attain a thickness of more than 250 km (Artemieva and Mooney, 2001). Velocity-depth profiles obtained from surface-wave analysis are not in question, but caution is required with the interpretation because averaging of velocity with distance along the path travelled by the seismic waves must be taken into account. The ability to resolve lateral changes in velocity also decreases with depth because, at deeper levels velocity is only constrained by surface waves of greater wavelength. Horizontal velocity variations on distances that are less than some small multiple of the seismic wavelength are simply not measurable using surface waves. Tomographic inversion tends to introduce further smoothing of the velocity field because the tomographic problem is intrinsically under-constrained.

In considering how to reconcile these different data and different interpretations of how the Tibetan lithosphere has been affected by the continental collision, we here revisit the convective thinning hypothesis proposed by Houseman et al. (1981) and England and Houseman (1989), but we amend one of their basic assumptions: we here allow for an intrinsic density difference between the sub-continental mantle lithosphere and the asthenosphere beneath. Jordan (1978) proposed that cratonic lithosphere must be stabilised against convective overturn in order to enable the long-term stability of these zones of thickened lithosphere in a concept termed the *isopycnic tectosphere*. He inferred the likely stabilisation mechanism to be density reduction caused by extraction of basalt melts. Based on xenolith analyses from a global catalogue, Poudjom Djomani et al. (2001) demonstrated that the density of depleted mantle lithosphere is intrinsically less than that of primitive upper mantle (McDonough and Sun, 1995), and moreover, that the density deficit increases with the tectonic age of the craton. Archaean-age cratons have mantle lithosphere with the most depleted (and most buoyant) signature. More recently active cratons may have been re-fertilized by metasomatism, causing a reduction in buoyancy, but Griffin et al. (2009) conclude that most Proterozoic-age cratons remain buoyant relative to primitive upper mantle. Kay and Mahlberg-Kay (1993) considered the impact of intrinsic buoyancy resisting or slowing delamination, but concluded that there is anyway extensive evidence for magmatism produced by delamination. In any case, a positively buoyant layer of mantle lithosphere might still be subject to gravitational instability even if it is not removed.

Because the density of Tibetan mantle lithosphere is not well constrained, we here compare calculations that simulate a gravitational instability developed within a mantle lithosphere layer which has an intrinsically lower density. We consider experiments with differing amounts of compositional buoyancy, and show that a positively buoyant layer of mantle lithosphere may remain in place, while undergoing comprehensive overturn. Using simplified numerical experiments which illustrate the process, we argue that the process is : (a) likely to have occurred beneath Tibet, given what we know of the relevant physical properties, (b) able to explain recent thermal rejuvenation and volcanism of the plateau without requiring the loss of lithospheric mantle beneath the plateau, (c) consistent with seismic velocity structure of the lithosphere in Tibet and surrounding regions, and (d) consistent with localised melting of mantle lithosphere, basaltic volcanism, and a rapid heating of the lower crust by plutonism.

Numerical Experiments

We consider a simplified two-dimensional system consisting of three layers of incompressible viscous fluid: crust (*cr*), above mantle lithosphere (*ml*), above asthenosphere (*as*). We want to investigate the case in which the middle layer is unstable due to a temperature-induced internal stratification of density decreasing with depth. The process that we describe below is essentially a Rayleigh-Taylor instability of the middle layer; for simplicity we neglect thermal diffusion in these experiments. Although doing so means that the instability may develop faster than the case where diffusion is included, the difference will be small because the time scale of interest (10 to 20 Myr) is small compared to the thermal time constant of the layer. The properties of the fluid (density and viscosity) are transported by the flow and we continuously track the internal distribution of density and viscosity as the instability develops. The two material interfaces representing the Lithosphere-Asthenosphere boundary (LAB) and the Moho are especially significant. Our aim here is to examine the consequences of the overturn of the mantle lithosphere and whether the process is consistent with geophysical and geochemical data from the Tibetan Plateau. We assume as a plausible example that the mantle lithosphere layer has a thickness L (nominally 160 km), the overlying crust has thickness $L/2$ and the thickness of asthenosphere above the transition zone is also L. Thus the model Moho is initially a uniform 80 km deep and the model LAB is 240 km deep.

We assume that this model starting condition has been produced by sustained convergence in the collision zone causing shortening and thickening of the lithospheric layers. To simplify, we assume the initial geotherm varies linearly with depth in the mantle lithosphere and is constant in the asthenosphere beneath. If the temperature at the LAB is nominally 1350°C and that at the Moho is 650°C (Fig. 2), the density difference between bottom and top of the middle layer $\Delta\rho_T$is a consequence of thermal expansion acting on a temperature contrast of order 700°C. For a thermal expansion coefficient of 3.5 x 10^{-5} K^{-1} (Bouhifd et al., 1996), the density increases from the LAB to the Moho by$\Delta\rho_T \approx 80\text{kg m}^{-3}$.

The lower layer representing asthenosphere is assumed to have a constant temperature and density but we allow for an intrinsic density difference between mantle lithosphere and asthenosphere attributed to geochemical depletion and represented by a step change in the initial density profile at the LAB: $\Delta\rho_C = \rho_{as} - \rho_{mlab}$. Based on the compilation of Griffin et al. (2009), $\Delta\rho_C$= 78 kg/m^3 is a representative estimate for the average reduction in density of mantle lithosphere of Archaean age relative to primitive upper mantle. This density contrast decreases to 40 kg/m^3 for mantle lithosphere of Proterozoic age, but Griffin et al. (2009) infer that the earliest Archean lithosphere was even more depleted and less dense. In the following calculations we consider a non-dimensional relative density profile scaled by $\Delta\rho_T$ (Fig. 2), such that $\rho'_{as} = 0$ in the lower layer, ρ'_{ml} varies linearly from $a = -\Delta\rho_C/\Delta\rho_T$ at the base of the mantle lithosphere ($z = L+h$) to $1+a$ at the top of the mantle lithosphere ($z = h$), and $\rho'_{cr} = (\rho_{cr} - \rho_{as})/\Delta\rho_T \approx -7.88$ in the crustal layer. We ignore variation of density within the crustal layer. Given the uncertainty in both thermal and intrinsic density contrasts, we treat the parameter a (the ratio of compositional to thermal density contrast between asthenosphere and mantle lithosphere layers) as a free parameter, and consider here values of $a = -1.5, -1,$and $- 0.5$(Fig. 2).

In these numerical experiments we assume a linear dependence of strain rate on deviatoric stress, but allow the viscosity coefficient to vary with position, and assume that the physical properties (density and viscosity) are advected by flow within the system of layers. The initial distribution of viscosity in the 3-layer system is based on an exponential decrease of viscosity with depth in both crust and mantle lithosphere layers. In each case we assume a factor of 10 decrease from top of the layer to base of the layer. The viscosity at the base of the crust is set to η_0, the same value as the viscosity at the base of the mantle lithosphere, and the same as the uniform viscosity assumed for the asthenosphere. Although aspects of the viscosity profile used here (Fig. 2) are ad hoc, and further experiments with different possible viscosity profiles may be called for, it is consistent with the idea of viscosity decreasing systematically with depth in both crust and mantle lithosphere, with lowermost crust being significantly weaker than uppermost mantle, and with the asthenosphere being relatively weak compared to uppermost mantle. The main effect of increasing the viscosity at any level in the model is to increase the time required for an instability to develop. In our calculations, viscosity is rendered dimensionless by η_0, distance by L, relative density by $\Delta\rho_T$, stress by $gL\Delta\rho_T$, time by $\eta_0/(gL\Delta\rho_T)$, and velocity by $(gL^2\Delta\rho_T)/\eta_0$. Thus, if $\eta_0 = 10^{20}$ Pa s, the time scale-factor is 0.025 Myr and the velocity scale factor is 6.45 m/yr.

We model a 2D region whose width is 6 times the thickness of the mantle lithosphere L (nominally 960 km). We assume the vertical side walls of the 2D region are reflecting boundaries, with zero vertical traction and zero horizontal velocity. We also set the upper and lower horizontal boundaries to zero horizontal traction and zero vertical velocity. We introduce a small perturbation to both density and viscosity fields from which instability can grow. This perturbation is ad hoc, but includes harmonic components of wavelength $12/n$, with integer $n = 1,2,3\ldots.8$. We thus allow the instability to favour the fastest growing wavelength for Rayleigh-Taylor instability from among the different components of the perturbation. Typically, the fastest growing instability has a wavelength about 3 times the unstable layer thickness; the other components of the perturbation also introduce some irregularity to the solution, but do not have a strong effect on the time required for the instability to develop.

The instability is allowed to develop by time-stepping, with the density and viscosity fields advected by the flow field computed at each time level. At each time-level, we balance stress gradients (pressure p, and deviatoric stress τ_{ij}) against body force (g_i), assuming inertial terms are negligible

$$\frac{\partial\tau_{ij}}{\partial x_j} + \frac{\partial p}{\partial x_i} + \rho g_i = 0, \quad (1)$$

and the plane-strain flow is incompressible:

$$\frac{\partial u_i}{\partial x_i} = 0 \tag{2}$$

for velocity components u_i, and rates of strain governed by a Newtonian viscosity law with spatially variable viscosity:

$$\tau_{ij} = \eta(x,y)\left(\frac{\partial u_i}{\partial x_j} + \frac{\partial u_j}{\partial x_i}\right) \tag{3}$$

The algorithm is implemented in the program *basil* (Houseman et al., 2008; Fang et al., 2024). The solver for the velocity field uses the finite element method applied on an irregular mesh of triangles using 6-node quadratic interpolation functions for velocity components and 3-node linear interpolation for pressure. The pressure discontinuity that is implied where there is a discontinuity of viscosity (e.g., across the Moho) is handled by duplicating the nodes on that boundary and adding another set of constraints to enforce continuity of velocity at those node pairs. The finite element mesh is advected with the flow, and when the mesh is sufficiently distorted, a new mesh is created respecting the current domain interfaces, and the current density and viscosity fields are interpolated on to the updated mesh. We track internal strain within the 2D flow field by advecting a set of initially circular markers that are deformed by the shear flow as they are translated.

The flow field that develops in the presence of this initial density distribution is dependent of course on the variation of viscosity η within the layers. Although there is no motive force for flow within the upper and lower layers owing to their initial uniform density, the developing instability in the middle layer necessarily induces flow in the layers above and below, due to variations of normal and shear stress developed on the interfaces. Deflections of the internal interfaces develop under the influence of the forces produced by the lateral density gradients as the gravitational instability develops. We neglect the impact of thermal diffusion in these calculations, based on the simplifying assumption that growth of the instability is rapid compared to the time scale for significant thermal diffusion to occur.

Results

The convective overturn that arises as a consequence of the experimental set-up is illustrated in Fig. 3 for a case where $a = 0$ (no compositional buoyancy) and sufficient time has elapsed for the initial instability to approach completion. This experiment illustrates the convective thinning of most of the mantle lithosphere in a period of about 10 Myr in a manner that is consistent with the convective thinning process described by Houseman et al. (1981). In these experiments we imposed a boundary at 400 km depth in order that the flow process occurring in the uppermost mantle can be better resolved, but it is expected that in reality any downward flow that reaches the upper mantle discontinuity at 410 km would likely continue sinking into the transition zone. The experiment shown in Fig. 3 has high viscosity (η' = 10) and high density ($\Delta\rho' = 1$) at the top of the mantle lithospheric layer, but much of the high viscosity material near the top of the layer is effectively removed by the instability. The relatively low viscosity of the lowermost crust is significant in enabling the high viscosity upper mantle to move laterally and, as it does so, to drag lower crust into a pile that pushes the Moho down and the Earth's surface upward, causing extensional strain in the upper crust above the loci of mantle downwelling. Between the downward push of thickened crust and pull of heavy mantle lithosphere, significant downward deflection of the Moho occurs.

In Figs. 4 and 5 we show the corresponding instability that develops for the three cases in which non-zero compositional buoyancy is assumed with a = -0.5, -1.0 or -1.5 for the initial density profiles illustrated in Fig. 2. In each of these experiments we used the same initial viscosity distribution and the same initial perturbation used in Fig. 3. For a = -1 or -1.5, the intrinsic density contrast between mantle lithosphere and asthenosphere is sufficient to preserve the separate layering, though relatively large displacements of the LAB interface occur as the instability develops, and minor entrainment of the asthenosphere through the mantle lithosphere can occur. When$a = -0.5$, a large fraction of the mantle lithosphere can penetrate the asthenosphere layer and sink to the transition zone, although the lower half of the *ml* layer is buoyant relative to the asthenosphere and resists entrainment. Comparing the case of a = -0.5 (Fig. 4a,5a) to that of a = 0 (Fig. 3), the instability takes almost twice as long and the final dominant wavelength is between about λ' = 1.5 and 2, rather than λ' = 3. The dominant wavelength for a = -1 or a = -1.5 is also between about λ' = 1.5 and 2. The selection of dominant wavelength reflects whether the circulation is restricted to the thinner *ml* layer by positive buoyancy, or involves both *ml* and *as* layers (effectively twice the thickness). We also considered the possibility that the instability with $a = -1$ might be able to develop at longer wavelengths, by repeating our experiment with short wavelength components of the initial perturbation removed, leaving harmonic perturbations that explicitly included wavelengths only of λ' = 6 and 12. We found that the instability developed more slowly and, even though the shorter wavelength perturbation was not present in the initial state, a secondary instability at the shorter wavelength developed (presumably from rounding noise). These tests imply that in the presence of a random perturbation that includes a broad range of harmonics, the instability in a positively buoyant layer will develop at a wavelength between 1.5 and 2 times the unstable layer thickness.

The thinning of the uppermost dense part of the mantle lithosphere between the downwelling sheets appears similar in all of these experiments. The residual parts of this layer have undergone extreme thinning by lateral stretching, as indicated by the horizontal elongation of the originally circular strain markers. Material that originated in the lower part of the mantle lithosphere is juxtaposed against this residual layer, bringing high temperatures close to the base of the crust. For *a* = 0 (Fig. 3) this hot material was originally asthenosphere, whereas for$a = -0.5$(Fig. 4,5) the asthenosphere is buffered by a considerable thickness (of order 50 km) of basal lithosphere that was relatively buoyant, and still relatively hot. Laterally averaged profiles of the density and viscosity (Fig. 6) provide another perspective on the redistribution of material in the *ml* layer. For a = -1 and -1.5, we see that the density vs depth profile within the *ml* layer is effectively inverted, leaving a relatively thin boundary layer of residual material at the top of the layer, and a more diffuse gradient at the base of the layer, related to the depth variation of the interface between *ml* and *as* layers after the instability has developed.

While the model LAB is completely disrupted in those experiments with *a* = 0 and *a* = -0.5, it is preserved in a very perturbed state with *a* = -1 and *a* = -1.5. Strong lateral gradients in the depth to the *ml/as* interface are possible when the asthenosphere density is close to the density of the material that was stripped from the uppermost mantle and ends up pooling near the base of the mantle lithosphere (Fig. 4,5b,c). With *a* = -1.5, there remains a significant density contrast across the LAB interface and its depth variation is smaller by about a factor of 2, though still in the range240 ± 20km(Fig. 4,5c). In both of these experiments, the strain markers show that the flow velocity is approximately parallel to the material interface and the up-slope flow of the overturning layer is shearing and dragging asthenosphere toward the shallowest part of the *as* layer beneath an upwelling material flow in the *ml* layer. While the resolution of the numerical experiments makes it difficult to quantify amounts and rates, it seems likely that this flow field would inject minor amounts of asthenospheric material into the upwelling flow in the *ml* layer, and rapidly transport it to the upper part of the *ml* layer.

The density contrast across the *cr*/*ml* interface is so much larger than that across the *ml/as* interface, that the deflection of the model Moho is much less than the deflection of the model LAB. Nonetheless, significant deflections of the Moho are represented in these models. The upward deflection of the Moho is of order 1.5 to 3 km over the extensive areas of upwelling, whereas localized downward cusps are deflected as much as 10 km beneath piles of hot lower crustal material that are swept into the sites above downwelling in the *ml* layer. The Moho deflection amplitudes are similar in the three experiments shown in Figs. 4,5 because in each case, the quantities of dense material in the sinking structures of the *ml* layer are similar. The variation in the normal stress on the upper surface of the model, which amounts to about 5 MPa (peak to peak) in each of these experiments, can be interpreted as a variation in the vertical deflection of the surface of order 200 m, with relative uplift occurring over areas where the crust is thickened. In Fig. 3 the greater dominant wavelength results in more material being entrained in each of the more widely-spaced downwellings and thus in greater deflection of the model Moho as the instability develops.

It is also notable that the extent to which the crustal layer is perturbed by the instability is similar in all three experiments shown in Figs. 4,5. The response of the crust to the thinning and downward transport of the uppermost *ml* layer is here dependent on the assumed low viscosity of the basal *cr* layer, but we found that whether the lower *cr* layer is weak or strong does not have a strong impact on the overturn of the *ml* layer.

Maps of the maximum shear strain rate and the maximum shear stress (Fig. 7 and Fig. 8) reveal other important aspects of how the instability develops. The two cases in which the instability is contained within the original *ml* layer are similar in showing that maximum shear strain rates (Fig. 7, left) are greatest (of order 1% per Myr) near the *ml/as* interface, especially near the convergent flow beneath the upwelling within the *ml* layer. The strain rate maps are evidently consistent with the extreme deformation indicated by the strain-markers in Figs. 4,5. High strain rates are also evident in the basal layer of the crust, where low-viscosity material is dragged along by higher viscosity material in the upper part of the *ml* layer. In contrast the maximum shear stress maps (Fig. 7, right), which are basically obtained as the product of maximum shear strain rate and local viscosity, present a different perspective. The stress-difference maps are dominated by high-stress (of order 20 MPa) regions where the upper high-viscosity part of the *ml* layer is pulling away from the Moho. Song and Klemperer (2024) have described clusters of sub-Moho earthquakes in west Tibet and beneath the High Himalaya in south Tibet, which they interpret as caused by drips of eclogite. The model presented here provides a possible explanation for such observations that does not require eclogite to drive the flow. The distribution of sub-Moho seismicity beneath Tibet would be diagnostic of differential deformation within the mantle lithosphere layer, but it is unclear whether mantle seismicity beneath other parts of Tibet is yet adequately known to provide a useful constraint. For $a = -0.5$ (Fig. 8) in which the flow is not contained within the *ml* layer, the dominance of the stresses at the separation point of downwelling and Moho is similar to that of Fig. 7, and high strain rates are again observed in the lower crust, but the maximum strain rates beneath the Moho now occur on the sides of the downwelling sheets where relatively buoyant material either side of the downwelling is resisting the downward drag of the dense material in the core of the structure.

Discussion

The concept of continental lithosphere being de-stabilised and removed by a process of delamination, convective thinning, or mantle drips has been explored by many authors in the past five decades, in the context of regions including the Colorado Plateau (Bird, 1979; Levander et al., 2011), Tibet (Houseman et al., 1981; England and Houseman, 1989; Molnar et al., 1993; Houseman and Molnar, 1996; Turner et al., 1996), South America (Garzione et al., 2006; Kay and Mahlburg-Kay, 1993; Andersen et al., 2022), the Sierra Nevada (Saleeby and Foster, 2004), Iran (e.g. Hatzfeld and Molnar, 2010; Zarunizadeh et al., 2024), the Anatolian Plateau (Göğüş et al., 2017), the Carpathians, (Lorinczi and Houseman, 2009), New Zealand (Stern et al., 2013), and the North China craton (Gao et al., 2002). At least in the Carpathian case (and probably elsewhere) it seems clear from seismic tomography that material removed from the lithosphere can reach and pond in the mantle transition zone (Dando et al., 2011; Ren et al., 2012).

Tibet seems to be an exceptional case; the seismic tomography suggests that most of the lithosphere has remained in place (Priestley et al., 2006) while magmatism implies that some form of gravitational instability in the upper mantle has occurred. We argue that this is most simply explained by the mantle lithosphere here having a compositional density deficit relative to the asthenosphere. We have sketched here the basic mechanical process of instability occurring within a layer of depleted mantle lithosphere. If there is sufficient intrinsic buoyancy, the mechanism described here permits the depleted layer to remain in place after overturn. The overturn of the layer moves hot material from near the base of the lithosphere, to near the base of the crust. As the hot mantle lithosphere rises, decompression melting can occur to produce mantle melts such as alkaline basalts; as the lower crust heats by conduction, plutonism producing more silicic melts is likely.

The time scale on which the overturn instability proceeds (Figs. 3-5) is proportional to the viscosity scale constant η_0. We do not consider this viscosity to be well constrained a priori, but it is apparent from these calculations that a value greater than about 10^{20} Pa s would slow the overturn so much that it would not proceed fast enough to explain what has happened in Tibet during the last 20 Myr or so. Although the intrinsic density of the Tibetan mantle lithosphere is also not well constrained by seismic velocity measurements, seismic tomography images based on surface wave analysis appear to show that the mantle lithosphere remains in place beneath Tibet, while the tectonic, volcanic and magmatic history imply that there has been a significant transfer of heat into the lithosphere. The simplest way to reconcile these observations is to conclude that the mantle lithosphere has experienced a gravitational instability, but has not sunk in to the underlying asthenosphere because of its compositional buoyancy. Although both density and viscosity values inferred here for the Tibetan mantle lithosphere layer are low compared to values estimated in other continental environments, these low values follow as a logical deduction if we accept the evidence that an in situ mantle overturn has occurred.

This type of mantle instability could easily be slowed to the point of irrelevance by the relatively high viscosities that are thought to characterise other thick continental cratons (Artemieva, 2011; Pearson et al., 2021), so why is this process more in evidence beneath Tibet ?

Two factors may be important: firstly, the externally imposed convergence of this region has maintained relatively high strain rates overs 10's of millions of years since the collision began. These large strain rates effectively decrease the viscosity of all lithospheric layers when power-law viscosity or high-temperature plasticity mechanisms become active, because of the non-linearity of the applicable rheological laws (Hirth and Kohlstedt, 2013). Secondly, the rate of growth of Rayleigh-Taylor instability increases directly in proportion to the thickness of the unstable layer (Conrad and Molnar, 1997); as the lithosphere thickened during the collision it became increasingly likely that the mantle lithosphere would overturn.

Although the experiments described here represent an instability in two dimensions, the development of Rayleigh-Taylor instability in three dimensions has the same initial growth rate for $k^2 = k_x^2 + k_y^2$ regardless of the relative contributions of k_x and k_y (the x and y wavenumber components of a harmonic perturbation that develops into a flow field). A random initial perturbation of the density structure in the Tibetan mantle lithosphere would result in a 3D instability developing (Kaus and Podladchikov, 2001), with multiple localized downwelling sites separating a greatly thinned mantle lid. However, these 2D simulations provide a reasonable guide to the behaviour of a 3D flow, including the time scale on which the instability develops, the typical horizontal separation of the vertical thermal structures, and the overall inversion of the average density and thermal structure caused by the overturn (Fig. 6). It seems unlikely that a mantle lithosphere instability affected the whole plateau at the same time. Chung et al. (2005) describe spatial and temporal variations in the magmatic activity that has impacted different parts of the plateau at different times. Such variations may be expected to arise from the natural variability of material properties and the tectonic structures developed when the major terranes were assembled and underwent collisional orogeny. Based on the compilation of Chung et al. (2005), one would infer that the Qiangtang and W. Yangtze were first affected by extensive magmatism in the Eocene and Oligocene, the Lhasa terrane during the Miocene, and the Songpan-Ganze and W. Qiantang since the mid-Miocene and into the Quaternary. Xia et al. (2023) also describe major variations in lithospheric thermal structure across the Plateau based on a synthesis of regional geophysical data, and identify the north-central Qiangtang and central Songpan-Ganzi Blocks as having an anomalously thin lithosphere.

While xenolith petrology (Pearson et al., 2021) has provided essential information about the composition and history of the continental lithosphere, the principal constraints on lithospheric structure and thickness come from seismology (Artemieva, 2011). Surface-wave tomography (Huang et al., 2003; Priestley et al., 2006; Shen et al., 2016) has provided the primary observation that the mantle lithosphere remains in place beneath Tibet, but it also reveals significant internal structure: slower velocities at around 100 km depth, above faster velocities at around 200 km. If temperature is the primary determinant of shear wave velocity (Priestley and McKenzie, 2013), this stratification is essentially consistent with the laterally averaged structure shown in Fig. 6 produced by overturn of the mantle lithosphere layer. Surface-wave tomographic models are constrained by the apparent propagation speed of dispersed wave-trains that comprise a range of periods. With increasing period, the eigenfunctions for Rayleigh wave propagation are more sensitive to structure at increasing depth, e.g. at 50 s period the phase velocity measurement is most sensitive to shear-wave velocity V_s at depths in the range of about 30-120 km while at 200 s period the sensitivity peaks at depths in the range of about 200-500 km (Ritzwoller and Levshin, 1998). Also increasing with period, the wavelength of 50 s (or 200 s) horizontally propagating Rayleigh waves is around 200 (or 800) km respectively, and hence the ability to resolve the kind of short wavelength lateral variation illustrated in Fig. 4 for the depth range 80-240 km is severely compromised, even if the path sampling is dense. Nonetheless, it is entirely plausible that the depth-variation of the horizontally averaged V_s structure within Tibet is well-resolved, and the observed structure appears consistent with that produced by the overturn of a gravitationally unstable mantle lithosphere. For upper mantle compositions, depletion has little impact on seismic velocity; the principal variations of velocity are determined by temperature (Schutt and Lesher, 2006). Thus a shear-wave velocity profile through the Tibetan upper mantle should detect the modelled inversion of temperatures within a depleted layer which has overturned if the compositional density contrast between the layers is sufficient to preserve the separation of mantle lithosphere from asthenosphere. Vertical sections by both Huang et al. (2003) and Priestley et al. (2006) indeed show the relatively low velocities below the crust, above a higher-velocity layer at depths between 150 and 200 km, before velocity again decreases in the asthenosphere.

While large lateral variations of depth to the LAB are expected when the compositional and thermal density contrasts are comparable (Fig. 4b,5b) it seems unlikely that these variations could be measured seismologically. However, the relatively narrow hot and cold vertical structures that cross the mantle lithosphere present a more feasible target for the technique of teleseismic body-wave tomography. Near-vertically propagating body waves, in principle, can provide the lateral resolution required to identify the velocity signature of these vertical structures given a sufficiently dense and broad-aperture seismic array, even if the technique is relatively insensitive to the depth variations of velocity revealed by the surface-wave studies. The temperature contrast between the hot and cold vertical structures in these calculations is similar to the temperature contrast between a subducted slab and ambient mantle, so the colder material is expected to have a P-wave velocity up to 4% greater than the hot material at the same pressure (Mao et al., 2015). For near vertically propagating P waves that pass through 100 km of the contrasting hot and cold structures we may see up to about 0.5 s difference in relative arrival time, allowing that lateral variations in Moho depth, crustal structure and topography on the LAB interface may complicate analysis.

Ren and Shen (2008) used finite frequency teleseismic tomography to derive images of the lateral variation of lithospheric structure in South-east Tibet, which show (at depths of 112 and 188 km) a remarkable pattern of alternating fast and slow regions. This pattern is vertically continuous, has a characteristic wavelength of 250-300 km and has an interpreted velocity contrast of about 1.5% between fast and slow regions. These strong lateral variations in V_p and V_s could be interpreted as revealing the loci of upwelling and downwelling within a destabilised mantle lithosphere layer. Moreover, Ren and Shen (2008) infer that the measured V_p/V_s ratios in the fast anomalies imply a highly melt-depleted mantle composition. More recently, Qu et al. (2020) reveal a similarly complex pattern of P-wave velocity variation across most of the Tibetan Plateau within the upper 200 km. Full-wave $\mathrm{P_n}$ tomography has also been applied by Bao and Shen (2018) to reveal structures in the upper mantle beneath eastern Tibet, which they associate with convective thinning or delamination processes.

Taken together, the surface wave models that show a laterally averaged stratification, and the teleseismic and full wave $\mathrm{P_n}$ tomography that shows relatively short-wavelength fast and slow regions within the mantle lithosphere, are consistent with the type of gravitational instability depicted in Figs. 4-5b,c. Both types of observation can be explained as the result of an overturn of the mantle lithosphere layer that has remained more or less in place beneath the Tibetan Plateau, constrained by its overall compositional buoyancy. Further analyses of the seismic signature of the Tibetan mantle lithosphere, including more extensive and better-resolved teleseismic body-wave tomography surveys, are needed to determine whether the structures imaged beneath the Tibetan plateau are actually diagnostic of the overturn of an unstable mantle lithosphere layer.

The hypothesised overturn of a relatively buoyant mantle lithosphere layer has a profound and relatively rapid effect on the subsequent thermal evolution of crust and mantle. As illustrated in Figs. 4 and 5, the overturn of the layer causes hot material from the base of the layer to be brought rapidly to near-Moho depths, separated from the crust only by a much thinned remnant of the colder material that was originally the uppermost layer of the mantle lithosphere. Conversely, the colder material is now ponded above the LAB. Although there is a very high degree of lateral variability in the geothermal state of the layer, Fig. 6 shows that the laterally averaged state is well-represented as a simple overturn of the original density profile in the depth range of the mantle lithosphere. Within the mantle lithosphere layer, both density and viscosity serve as proxies of temperature, as shown in Fig. 2, and we can consider the subsequent impact of thermal diffusion on the overturned state, by solving the one-dimensional thermal diffusion equation (details in Appendix) to examine how the average geotherm evolves following the overturn.

Figure 9 shows the evolution of that idealised average geotherm in the first 16 Myr following the initial perturbed state that represents the post-overturn layer. Assuming a constant LAB temperature of 1350°C, heat flows into the base of the layer from the asthenosphere. Similarly, heat flows into the base of the crust (initially at 650°C) from the uppermost mantle lithosphere. The heat flowing into the mantle lithosphere causes a net increase in the average temperature of the whole lithosphere, because it takes much longer for heat to exit the system through the Earth's surface. In this case the thermal content peaks at about 40 Myr before gradually decaying back to the pre-overturn geotherm on a time-scale of about 500 Myr. The increase in mean temperature of the whole lithosphere causes thermal expansion and, under isostatic conditions, the surface elevation of the region rises by about 600 m, most of which occurs in the first 10 Myr following overturn (details in Appendix).

The increase in surface elevation causes an increase in gravitational potential energy that would promote east-west extension in southern Tibet. The link between lithospheric heating and extension in Tibet was originally proposed by England and Houseman (1989) as evidence of a convective thinning event that removed a large fraction of the mantle lithosphere. Although oxygen isotope measurements of basin sediments from Central Tibet (Rowley and Currie, 2006) appear inconsistent with the uplift estimates of England and Houseman (1989), they are not inconsistent (Molnar et al., 2006) with the 600 m estimate obtained here for layer overturn rather than removal. An average increase of 600 m in elevation of the plateau increases the vertical stress component through the upper 160 km of the column of lithosphere by about 20 MPa, causing an increase in the gravitational potential energy (GPE) of order 3 x 10^{12} Nm^{-1}. This change in GPE is relatively large compared to the present force per unit length acting on the Himalayan boundary (estimated at about 8 x 10^{12} Nm^{-1} by Molnar et al., 1993), and thus provides a plausible explanation of why the plateau which developed in a north-south convergent setting switched to east-west extension in the mid-Miocene (England and Houseman, 1989).

The evolution of the average geotherm following overturn of the layer in the simplified model shows that average temperatures at the base of the crust could rise from the initial 650°C to about 900°C within the first 5 Myr or so and would be sustained at that level for about 20 Myr before slowly falling again. One might therefore expect a pulse of felsic magmatism and plutonism with melt generated in the lower crust following the convective overturn of the mantle lithosphere (Platt and England, 1994). The evidence that Tibetan crust has been extensively affected by plutonism is provided by measurements of high seismic wave attenuation and zones of high electrical conductivity in the crust, as summarized by Klemperer (2006). Moreover, the possible mechanical effects of upper mantle overturn on the base of the crust, as seen in the displacement of strain markers and isotherms of Figs. 4 and 5, suggest that plutonic activity within the crust should be correlated with the distribution of upwelling and downwelling in the overturning layer beneath, as suggested by Molnar (2014).

Pulses of alkaline volcanism require a somewhat different mechanism, but an explanation is seen in the likely minor entrainment of asthenospheric melt in the middle of the upwelling regions of the overturning mantle lithosphere layer (Figs. 4 and 5). Such material is fairly rapidly propelled to near sub-crustal depths; the maximum upward velocity in the $a = -1$ case of Figs. 4 and 5 scales to about 20 km/Myr, without considering any additional buoyancy that may be generated by melting. In this environment, entrained material is likely to undergo decompression melting as it approaches the crustal interface, possibly mixing with metasomatised mantle in that layer to give the characteristic high-K signature of Tibetan basalts (Turner et al., 1996; Chung et al., 2005; Ding et al., 2003).

Simple models of a structure the size of the Tibetan Plateau are only plausible when one puts aside the multitude of details that are known from surface observations and geophysical measurements, but we acknowledge the many contributions of thousands of geologists and geophysicists whose observations can be used to test the validity of any model. Reviews like those of (Yin and Harrison, 2000; Yin, 2006; Klemperer, 2006; Kapp and DeCelles, 2019) help us to see the themes below the detail and we acknowledge here the encyclopedic grasp of Tibetan geology by An Yin. His recent passing and those of other major figures like Peter Molnar, and Paul Tapponnier, represent a major loss to the community, but we celebrate their huge contributions to our understanding of the Tibetan Plateau.

Conclusions

The geological evolution of Tibet in the past ~50 Myr is dominated by magmatism, crustal thickening and deformation which has affected the entire region. The activation of normal faulting in Tibet since about 10-15 Ma is one indication that a rapid and significant change in the stress state of the Tibetan lithosphere occurred at about that time. The widely accepted idea that a Rayleigh-Taylor type instability caused dense viscous mantle lithosphere to sink through the upper mantle and be replaced by asthenosphere has been disputed because seismic velocity measurements show fast, cold material at depths of 200 km or more beneath much of the plateau. Instead, we show here that an internal convective overturn of a relatively buoyant Tibetan mantle lithosphere can explain both the seismic shear wave velocity distribution and a recent rapid evolution of the thermal, magmatic and tectonic state of the Tibetan lithosphere. The models described here point to the need for further detailed teleseismic body-wave tomography of the entire Tibetan plateau and the need for further modelling of how asthenospheric material can be entrained and rapidly transported through the mantle lithosphere to produce basaltic melts that reach the surface.

Acknowledgments

This paper has been in development for too many years, but it has benefited very much from discussions with various people including Peter Molnar, Simon Turner, Tim Stern, and Kevin Burke whose comment along the lines of “why do you call this layer lithosphere ?” is entirely apt. We thank Editor A. Zuza, reviewer O. Göğüş, and one anonymous reviewer for constructive comments. The *basil* software library used for the viscous flow calculations is available at: https://github.com/greg-houseman/basil

Appendix: Thermal evolution calculation

The one-dimensional thermal diffusion process is governed by

$$\frac{\partial T}{\partial t} = \kappa \frac{\partial^2 T}{\partial z^2} + H \tag{A1}$$

where T is temperature, z is depth, t is time, κ is the thermal diffusivity and H represents a rate of heating caused by radioactive decay, assumed constant in the crustal layer and assumed zero in the mantle lithosphere. The equilibrium solution to this equation $T_{\mathrm{eq}}(z)$ is the quadratic equation represented in Fig. 2 assuming temperature at the Moho ($z = h$) of T_{M} and temperature at the base of the lithosphere ($z = h+L$) of T_{L}. The general solution to the time-dependent problem is represented using a Fourier series:

$$T = T_{eq}(z) + \sum_{n=1}^{\infty} A_n \sin\left(\frac{n\pi z}{L+h}\right) \exp\left(\frac{-\kappa n^2 \pi^2}{(L+h)^2} t\right) \tag{A2}$$

and the coefficients A_n are evaluated using:

$$A_n = \frac{2}{L+h} \int_{z=0}^{L+h} (T_0 - T_{eq}) \sin\left(\frac{n\pi z}{L+h}\right) dz \tag{A3}$$

where T_0 is the immediate post-overturn profile represented in Fig. 9. As the form of the initial thermal transient is simple, the A_n coefficients can be evaluated analytically:

$$A_n = \frac{2(T_L - T_M)}{n\pi} \left[-1 - \cos\left(\frac{Ln\pi}{L+h}\right) + 2\left(\frac{L+h}{Ln\pi}\right) \sin\left(\frac{Ln\pi}{L+h}\right)\right] \tag{A4}$$

To calculate the effect on surface uplift, the depth integral of density at time t, relative to that at time zero is:

$$\int_0^{L+h} \rho\alpha(T_0 - T(t))dz = \int_0^{L+h} \rho\alpha \sum_{n=1}^{\infty} A_n \sin\left(\frac{n\pi z}{L+h}\right) \left[1 - \exp\left(\frac{-\kappa n^2 \pi^2}{(L+h)^2} t\right)\right] dz \tag{A5}$$

which evaluates as:

$$\int_0^{L+h} \rho\alpha(T_0 - T(t))dz = 2\rho_m \alpha (L+h) \sum_{n=0}^{\infty} \left(\frac{A_{2n+1}}{(2n+1)\pi}\right) \left[1 - \exp\left(\frac{-\kappa (2n+1)^2 \pi^2}{(L+h)^2} t\right)\right] \tag{A6}$$

Following the logic of McKenzie (1978), the changing density in the column produces a change, Δe, in surface level (relative to that at time zero):

$$\Delta e = -\frac{2\rho_m \alpha(L+h)}{\rho_c} \sum_{n=0}^{\infty} \left(\frac{A_{2n+1}}{\pi(2n+1)}\right) \left[1 - \exp\left(\frac{-\kappa(2n+1)^2\pi^2}{(L+h)^2} t\right)\right] \qquad \text{(A7)}$$

For Fig. 9, we used $L = 160$ km, $h = 80$ km, $\kappa = 10^{-6}$ m^{2}s^{-1}, $\rho_c = 2700$ kg m^{-3}, and $\alpha = 3.5 \times 10^{-5}$ K^{-1}.

References

Argand, E., 1924. La tectonique de l' Asie. *Proc. 13th Int. Geol. Cong.*, vol. 7, pp. 171 – 372.

Andersen, J., O.H. Göğüş, R.N. Pysklywec, T. Santimano, and E. Şengül Uluocak, 2022. Symptomatic lithospheric drips triggering fast topographic rise and crustal deformation in the Central Andes, Communications Earth & Environment, 3, 150. ttps://doi.org/10.1038/s43247-022-00470-1

Armijo, R., P. Tapponnier, J. L. Mercier, and H. Tong-Lin, 1986. Quaternary extension in southern Tibet: Field observations and tectonic implications, *J. Geophys. Res.*, 91, 13,803-13,872.

Artemieva, I. M., 2011. *The Lithosphere: An Interdisciplinary Approach*, Cambridge Univ. Press.

Artemieva, I.A. and W.D. Mooney, 2001. Thermal thickness and evolution of Precambrian lithosphere: A global study, *J. Geophys. Res*. 106, 16,387-16,414.

Bao X. and Y. Shen, 2020. Early-stage lithospheric foundering beneath the eastern Tibetan Plateau revealed by full-wave Pn tomography. *Geophys. Res. Lett*., 47, e2019GL086469, doi:10.1029/2019GL086469v

Bird, P., 1979. Continental delamination and the Colorado Plateau, *J. Geophys. Res*., 84, 7561-7571.

Bouhifd, M.A, D. Andrault, G. Fiquet, and P. Richet, 1996. Thermal expansion of forsterite up to the melting point, *Geophys. Res. Lett.*, 23, 1143-1146.

Burchfiel, B.C., L.H. Royden, R.D. van der Hilst, B.H. Hager, Z. Chen, R.W. King, C. Li, J. Lü , H. Yao and E. Kirby, 2008. A geological and geophysical context for the Wenchuan earthquake of 12 May 2008, Sichuan, People's Republic of China, *GSA Today*, v. 18, no. 7, doi:10.1130/GSATG18A.1

Chung, S., M. Chu, Y. Zhang, Y. Xie, C. Lo, T. Lee, C. Lan, X. Li, Q. Zhang and Y. Wang, 2005. Tibetan tectonic evolution inferred from spatial and temporal variations in post-collisional magmatism, *Earth-Science Reviews,* 68, 173 – 196. doi:10.1016/j.earscirev.2004.05.001

Conrad, C.P. and P. Molnar, 1997. The growth of Rayleigh-Taylor-type instabilities in the lithosphere for various rheological and density structures, *Geophys. J. Int.*, 129, 95-112.

Dando, B.D.E, G.W. Stuart, G.A. Houseman, E. Hegedus, E. Bruckl and S. Radovanovic, 2011. Teleseismic tomography of the mantle in the Carpathian-Pannonian region of central Europe, *Geophys. J. Int.*, **186**, 11-31. doi: 10.1111/j.1365-246X.2011.04998.x

Ding, L., P. Kapp, D. Zhong and W. Deng, 2003. Cenozoic Volcanism in Tibet: Evidence for Transition from Oceanic to Continental Subduction, *J. Petrology*, 44, 1833-1865. 10.1093/petrology/egg061

England, P. and G. Houseman, 1989. Extension During Continental Convergence, with Application to the Tibetan Plateau, *J. Geophys. Res*., 94, B12, 17,561-17,579.

England, P., and P. Molnar, 2005. Late Quaternary to decadal velocity fields in Asia, *J. Geophys. Res*., 110, B12401, doi:10.1029/2004JB003541

Fang, J., G.A. Houseman, T.J. Wright, L.A. Evans, T.J. Craig, J.R. Elliott and A. Hooper,The Dynamics of the India-Eurasia Collision: Faulted Viscous Continuum Models Constrained by High-Resolution Sentinel-1 InSAR and GNSS Velocities, *J. Geophys. Res.: Solid Earth*, 129, doi:10.1029/2023JB028571

Gan, W., P. Molnar, P. Zhang, G. Xiao, S. Liang, and K. Zhang, Z. Li, K. Xu, and L. Zhang, 2021. Initiation of Clockwise Rotation and Eastward Transport of Southeastern Tibet Inferred from Deflected Fault Traces and GPS Observations, *Geology*, https://doi.org/10.1130/B36069.1

Gao, S., R.L. Rudnick, R.W. Carlson, W.F. McDonough, and Y.S. Liu, 2002. Re-Os evidence for replacement of the original mantle lithosphere beneath the North China craton. *Earth Planet. Sci. Lett.* 198, 307–322 (2002).

Gao, R., H. Wang, A. Yin, S. Dong, Z. Kuang, A.V. Zuza, W. Li, and X. Xiong, 2013. Tectonic development of the northeastern Tibetan Plateau as constrained by high-resolution deep seismic reflection data, *Lithosphere*, 5, no. 6, p555–574.

Ge, W.-P., P. Molnar, Z.-K. Shen, and Q. Li, 2015. Present-day crustal thinning in the southern and northern Tibetan Plateau revealed by GPS measurements, *Geophys. Res. Lett*., 42, 5227–5235, doi:10.1002/2015GL064347.

Garzanti, E., 2008. Comment on "When and where did India and Asia collide?" by Jonathan C. Aitchison, Jason R. Ali, and Aileen M. Davis, *J. Geophys. Res*., 113, B04411, doi:10.1029/2007JB005276

Garzione, C.N., P. Molnar, J.C. Libarkin, and B.J. MacFadden, 2006. Rapid late Miocene rise of the Bolivian Altiplano: Evidence for removal of mantle lithosphere, *Earth and Planetary Science Letters*, 241(3–4), 543–556. https://doi.org/10.1016/j.epsl.2005.11.026

Göğüş, O.H., R.N Pysklywec, A.M.C. Şengör and E. Gün, 2017. Drip tectonics and the enigmatic uplift of the Central Anatolian Plateau, *Nature Communications*, 8, 1538, doi:10.1038/s41467-017-01611-3

Griffin, W.L., S.Y. O'Reilly, J. C. Afonso and G. C. Begg, 2009. The Composition and Evolution of Lithospheric Mantle: a Re-evaluation and its Tectonic Implications, *J. Petrology*, 50, 1185-1204. doi:10.1093/petrology/egn033

Hatzfeld, D., and P. Molnar, 2010. Comparisons of the kinematics and deep structures of the Zagros and Himalaya and of the Iranian and Tibetan plateaus and geodynamic implications, *Rev. Geophys.*, 48 (2), RG2005, doi:10.1029/2009RG000304

Hirth, G. and D. Kohlstedt, 2013. Rheology of the Upper Mantle and the Mantle Wedge: A

View from the Experimentalists. In: Eiler, J. (Ed.), *Inside the Subduction Factory*, American Geophysical Union. doi:https://doi.org/10.1029/138GM06

Houseman, GA; Barr TD; Evans, LA (2008) Basil: stress and deformation in a viscous material (Ch 3.8, pp77-85) in *Microdynamics Simulation,* ed. Bons, PD.; Koehn, D; Jessell, MW, Lecture Notes in Earth Sciences, **106**, Springer. ISBN: 978-3-540-25522-255

Houseman, G.A., D.P. McKenzie, and P. Molnar, 1981. Convective instability of a thickened boundary layer and its relevance for the thermal evolution of continental convergent belts, *J. Geophys. Res.*, 86, 6115-6132.

Houseman, G.A. and P. Molnar, 1996. Gravitational (Rayleigh-Taylor) instability of a layer with non-linear viscosity and convective thinning of continental lithosphere, *Geophys. J. Int.*, 128, 125-150

Huang, Z., W. Su, Y. Peng, Y. Zheng and H. Li, 2003. Rayleigh-wave tomography of China and adjacent regions, *J. Geophys. Res.*, 108, 2073, doi:10.1029/2001JB001696

Jordan, T.H., 1978. Composition and development of the continental tectosphere, *Nature*, 274, 544-548.

Kapp, P. and P.G. DeCelles, Mesozoic-Cenozoic geological evolution of the Himalayan-Tibetan orogen and working tectonic hypotheses, 2019. *American Journal of Science*, 319, 159 –254, doi:10.2475/03.2019.01

Kaus, B.J.P. and Y.Y. Podladchikov, 2001. Forward and Reverse Modeling of the Three-Dimensional Viscous Rayleigh-Taylor Instability, *Geophys. Res. Lett.*, 28, 1095-1098.

Kay, R.W. and S. Mahlburg-Kay, 1993. Delamination and delamination magmatism. In: A.G. Green, A. Kroner, H.-J. Gotze and N. Pavlenkova (Eds.), Plate Tectonic Signatures in the Continental Lithosphere. *Tectonophysics*, 219, 177-189.

Kind, R., and X. Yuan, 2010. Seismic Images of the Biggest Crash on Earth, *Science*, 329, 1479-1480. doi:10.1126/science.1191620

Klemperer S.L., 2006. Crustal flow in Tibet: geophysical evidence for the physical state of Tibetan lithosphere, and inferred patterns of active flow, *in*: Law, R.D., M.P. Searle and L. Godin,(eds.) Channel Flow, Ductile Extrusion and Exhumation in Continental Collision Zones. *Geological Society, London, Special Publications*, 268, 39–70.

Levander, A., B. Schmandt, M.S. Miller, K. Liu, K.E. Karlstrom, R.S., Crow, C.-T.A. and E.D. Humphreys, 2011. Continuing Colorado Plateau uplift by delamination-style convective lithospheric downwelling. *Nature* **472**, 461–465.

Lorinczi, P., and G.A. Houseman, 2009. Lithospheric gravitational instability beneath the Southeast Carpathians, *Tectonophysics*, **474(1-2)**, pp322-336. doi:10.1016/j.tecto.2008.05.024

Mao, Z., D. Fan, J.F. Lin, J. Yang, S.N. Tkachev, K. Zhuravlev and V.B. Prakapenka, 2015.

Elasticity of single-crystal olivine at high pressures and temperatures, *Earth and Planetary Science Letters,* 426, 204–215.

McDonough, W.F. and S. Sun, 1995. The composition of the Earth, *Chem. Geol.* 120, 223-253.

McKenzie, D.P., 1978. Some remarks on the development of sedimentary basins, *Earth and Planetary Science Letters*, 40, 25-32.

Molnar, P., 2004. Gravitational instability of mantle lithosphere and core complexes, *Tectonics*, 34, 478–487, doi:10.1002/2014TC003808

Molnar, P., P. England, and J. Martinod, 1993. Mantle dynamics, uplift of the Tibetan Plateau and the Indian monsoon, *Reviews of Geophysics*, 31, 357-395.

Molnar, P., G.A. Houseman and P.C. England, 2006. Palaeo-altimetry of Tibet, *Nature*, 444, E4, doi:10.1038/nature05368

Nábelek, J., G. Hetényi, J. Vergne, S. Sapkota, B. Kafle, M. Jiang, H. Su, J. Chen, B. Huang, and the Hi-CLIMB Team, 2009. Underplating in the Himalaya-Tibet Collision Zone Revealed by the Hi-CLIMB Experiment, *Science,* 325, 1371 (2009); doi: 10.1126/science.1167719

Ou, Q., S. Daout, J. R. Weiss, L. Shen, M. Lazecký, T.J. Wright, T. J., and B.E. Parsons, 2022. Large-scale interseismic strain mapping of the NE Tibetan Plateau from Sentinel-1 interferometry, *J. Geophys. Res*. Solid Earth, 127, e2022JB024176. https://doi.org/10.1029/2022JB024176

Pearson, G.D., J.M. Scott, J. Liu, A. Schaeffer, L.H. Wang, J. van Hunen, K. Szilas, T. Chacko and P.B. Kelemen, 2021. Deep continental roots and cratons, *Nature*, 596, 199-211. doi:10.1038/s41586-021-03600-5

Platt J.P., and P.C. England, 1994. Convective removal of lithosphere beneath mountain belts: thermal and mechanical consequences, *Am. J. Sci.*, 294, 307-336.

Poudjom Djomani, Y.H., S.Y. O'Reilly, W.L. Griffin and P. Morgan, 2001. The density structure of subcontinental lithosphere through time, *Earth Planet. Sci. Lett*., 184, 605-621.

Priestley, K., E. Debayle, D. McKenzie, and S. Pilidou, 2006. Upper mantle structure of eastern Asia from multimode surface waveform tomography, *J. Geophys. Res.*, 111, B10304, doi:10.1029/2005JB004082.

Priestley, K. and D. McKenzie, 2013. The relationship between shear wave velocity, temperature, attenuation and viscosity in the shallow part of the mantle, *Earth planet. Sci. Lett.*, 381, 78-91, doi:10.1016/j.epsl.2013.08.022

Qu, C., Y. Xu, W.C. Yang, et al., 2020. P-wave velocity imaging and lithospheric structure of the Tibetan Plateau, *Chinese J. Geophys.* (in Chinese), 63 (3), 847-859, doi:10.6038/cjg2020N0107

Ren, Y., G.W. Stuart, G.A. Houseman, B.D. Dando, C. Ionescu, E. Hegedus, S. Radovanovic, Y. Shen, and SCP Working Group, 2012. Upper mantle structures beneath the Carpathian-

Pannonian region: Implications for the geodynamics of continental collision, *Earth Planet. Sci. Lett.*., **349-350**, 139-152. doi:10.1016/j.epsl.2012.06.037

Ren, Y., and Y. Shen, Finite frequency tomography in south-eastern Tibet: Evidence for the causal relationship between mantle lithosphere delamination and the north–south trending rifts , *J. Geophys. Res.*, 113, B10316, doi:10.1029/2008JB005615

Ritzwoller, M.H. and A.L. Levshin, 1998. Eurasian surface wave tomography: Group velocities, *J. Geophys. Res*., 103, 4839-4878.

Rowley, D.B. and B.S. Currie, 2006. Palaeo-altimetry of the late Eocene to Miocene Lunpola basin, central Tibet, *Nature*, 439, 677–681, doi:10.1038/nature04506

Saleeby, J. and Z. Foster, 2004. Topographic response to mantle lithosphere removal in the southern Sierra Nevada region, California. *Geology* 32, 245–248.

Schutt, D.L. and C.E. Lesher, 2006. Effects of melt depletion on the density and seismic velocity of garnet and spinel lherzolite, J. Geophys. Res., 111, B05401, doi:10.1029/2003JB002950

Shen, W., M. Ritzwoller, D. Kang, Y. Kim, F. Lin, J. Ning, W. Wang, Y. Zheng and L. Zhou, 2016. A seismic reference model for the crust and uppermost mantle beneath China from surface wave dispersion, *Geophys. J. Int*. 206, 954–979. doi: 10.1093/gji/ggw175

Song, X. and S.L. Klemperer, 2024. Numerous Tibetan lower-crustal and upper-mantle earthquakes, detected by Sn/Lg ratios, suggest crustal delamination or drip tectonics, *Earth Planet. Sci. Lett.,* 626,118555.

Stern, T., G.A. Houseman, M. Salmon and L. Evans, 2013. Instability of a lithospheric step beneath western North Island, New Zealand, *Geology*, **41**, pp.423-426. doi: 10.1130/G34028.1

Styron,R.H., M.H. Taylor, K.E. Sundell, D. F. Stockli, J.A.G. Oalmann, A. Möller, A.T. McCallister, D. Liu and L. Ding, 2013. Miocene initiation and acceleration of extension in the South Lunggar rift, western Tibet: Evolution of an active detachment system from structural mapping and (U-Th)/He thermochronology, *Tectonics*, 32, 880–907, doi:10.1002/tect.20053

Tapponnier, P., and P. Molnar, 1977. Active Faulting and Tectonics in China, *J. Geophys. Res.*, 82, 2905-2930.

Turner, S., N. Arnaud, J. Liu, N. Rogers, C. Hawkesworth, N. Harris, S. Kelley, P. Van Calsteren, and W. Deng, 1996. Post-collision, shoshonitic volcanism on the Tibetan Plateau: Implications for convective thinning of the lithosphere and the source of ocean island basalts, *J. Petrol.*, 37, 5-71.

Turner, S., C. J. Hawkesworth, J. Liu, N. Rogers, S. Kelley, and P. van Calsteren, 1993. Timing of Tibetan uplift constrained by analysis of volcanic rocks. *Nature,* 364, 50-53.

Xia, B., I.M. Artemieva, H. Thybo, and S.L. Klemperer, 2023. Strong variability in the thermal structure of Tibetan lithosphere. *Journal of Geophysical Research: Solid Earth*, 128, e2022JB026213. https://doi.org/10.1029/2022JB026213

Yin, A., 2006. Cenozoic tectonic evolution of the Himalayan orogen as constrained by along-strike variation of structural geometry, exhumation history, and foreland sedimentation, *Earth-Science Reviews*, 76, 1 – 131.

Yin, A. and T. M. Harrison, 2000. Geologic evolution of the Himalayan-Tibetan orogen, *Annu. Rev. Earth Planet. Sci.*, 28, 211–80.

Yuan, X., J. Ni, R. Kind, J. Mechie, and E. Sandvol, 1997. Lithospheric and upper mantle structure of southern Tibet from a seismological passive source experiment. *J. Geophys. Res.*, 102, B12, 27491-27500.

Zarunizadeh, Z., K. Motaghi, R. Movaghari, Y. Yang, and K. Priestley, 2024. Seismological constraints on the lithosphere-asthenosphere system beneath the central and east Iranian Plateau, *Tectonophysics,* 873, 230225.

Zhang, Z., Y. Deng, J. Teng, C. Wang, R. Gao, Y. Chen and W. Fan, 2011, An overview of the crustal structure of the Tibetan plateau after 35 years of deep seismic sounding, *J. Asian Earth Sci.*, 40, 977–989.

Figures follow

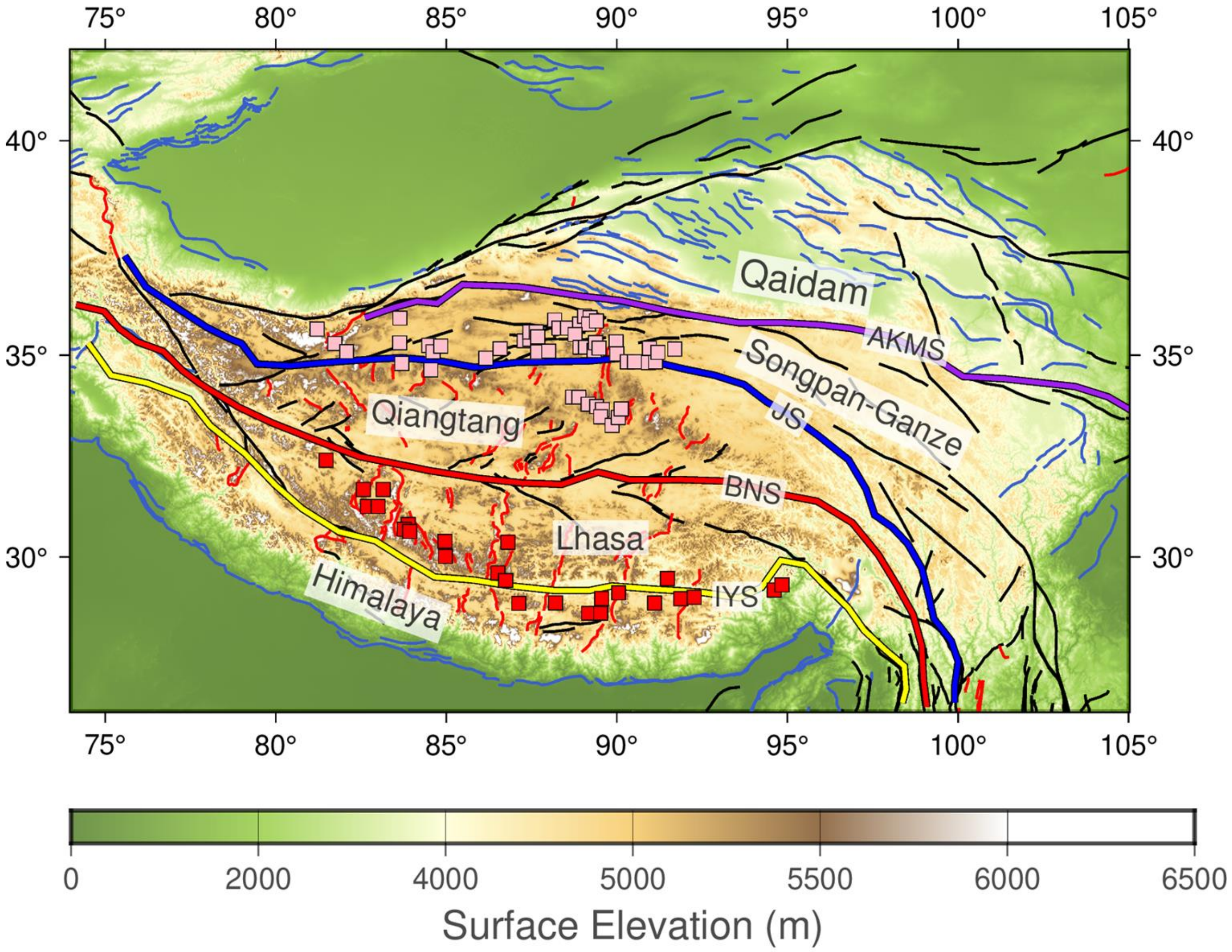

Figure 1. Simplified tectonic and topographic map of the Tibetan Plateau. The major terranes are labelled, separated by sutures resulting from closure of Paleo-Tethys and Neo-Tethys. Abbreviations: AKMS: Anyemaqen suture, JS: Jinsha suture BNS: Bangong–Nujiang suture, IYS: Indus–Yarlung suture. Black/red/blue lines show the locations of active strike-slip/normal/reverse faults from the GEM database https://www.globalquakemodel.org/product/active-faults-database. Squares show locations of Oligocene—Middle-Miocene (pink) and Middle-Miocene—Quaternary (red) volcanism (Chung et al., 2005).

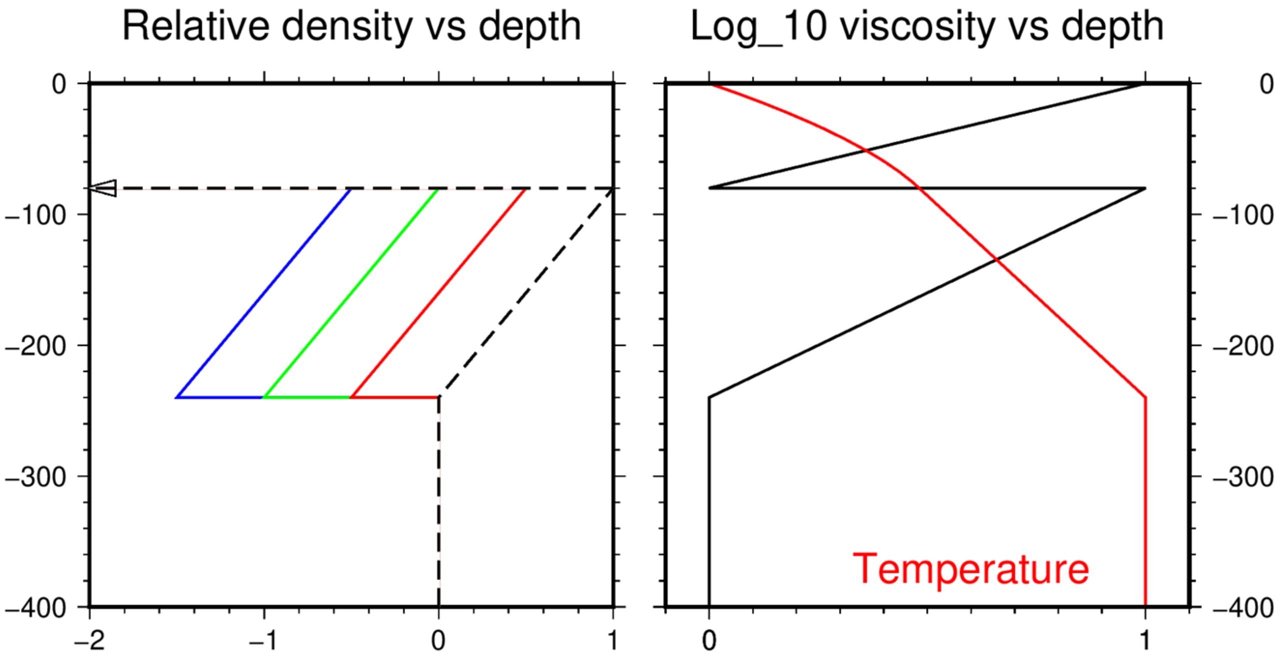

Figure 2. (left) Relative density (dimensionless) vs depth (km) for model cases with a = -0.5 (red), -1 (green), -1.5 (blue), relative to the case in which a = 0 (no intrinsic density contrast; dashed line). The density gradient in the depth range 80-240 km is attributed to thermal expansion dependent on the temperature profile, and the relative density contrast of 1 unit corresponds to about 80 km m^{-3}. (right) Dimensionless temperature (red) and log$_{10}$ of dimensionless viscosity (black) as used in the model calculations shown in the following figures. The assumed thermal profile is based on an equilibrium geotherm for a crustal layer which includes constant radioactive heating sufficient to result in a Moho temperature of 650ºC at 80 km, relative to the assumed LAB temperature of T_a = 1350ºC at 240 km.

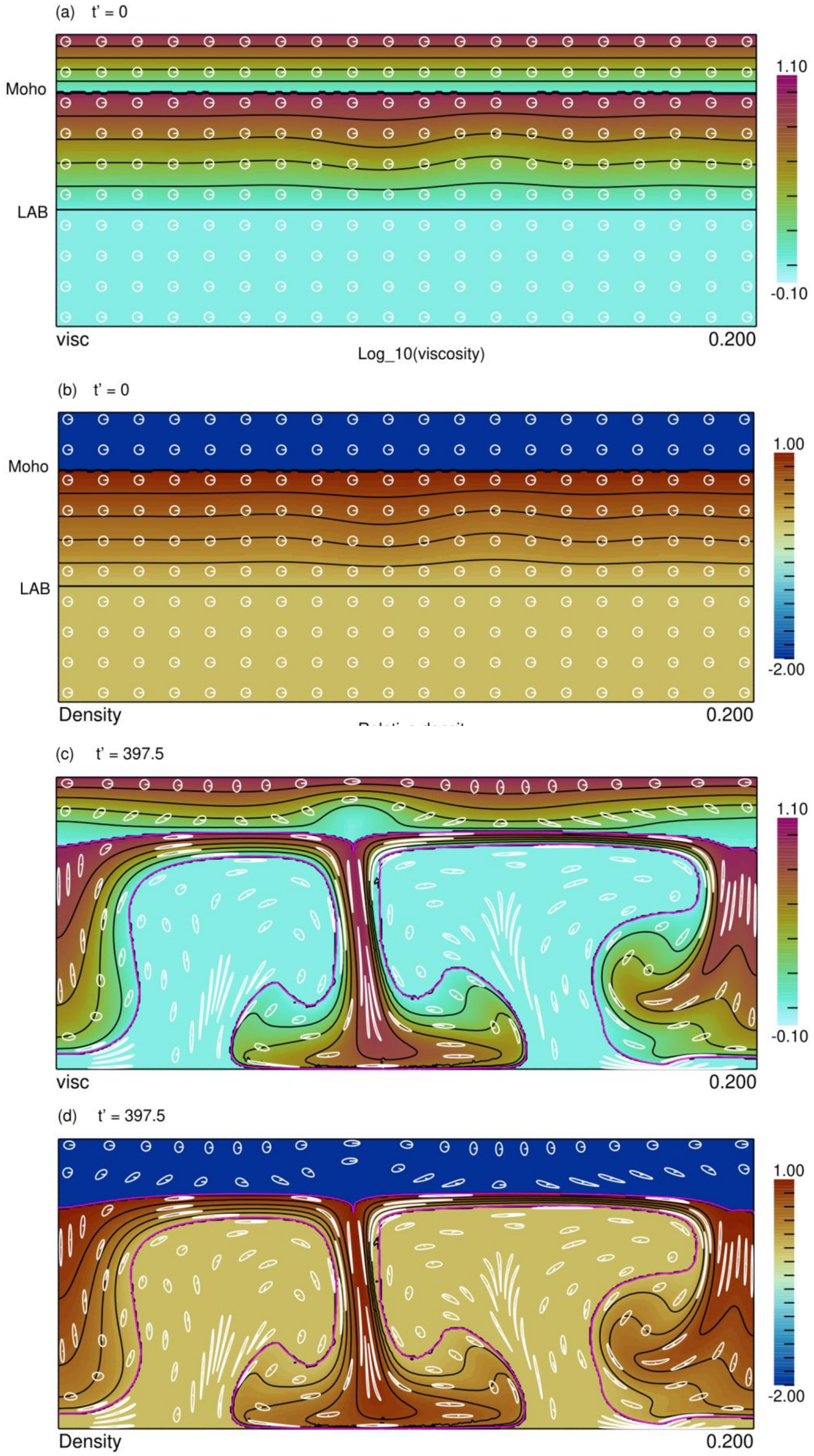

Figure 3. Colour maps show 2D section through idealized model of crust and upper mantle to a nominal total depth of 400 km with no compositional density contrast at the *LAB* for (a) viscosity and (b) relative density, at the initial state *t'* = 0, and (c) viscosity and (d) relative density, for the

evolved instability at $t' = 397.5$ (9.9 Myr for $\eta_0 = 10^{20}$ Pa s). For a,c the colour represents $\log_{10}(\eta/\eta_0)$ with values ranging between 0 ($\eta' = 1$) and 1 ($\eta' = 10$) with an exponential dependence on depth across crust (initially 80 km thick) and mantle lithosphere (initially 160 km thick). For b,d colour represents density relative to asthenosphere, with $\rho' = 0$ in the asthenosphere. Relative density varies between 0 and 1 across the mantle lithosphere and is off-scale in the crust at -7.88. The initially circular markers that are transported and deformed by the mantle flow illustrate the local strain produced by the flow. The magenta contours in c,d mark the major material boundaries (Moho, LAB) that separate mantle lithosphere from crust and asthenosphere.

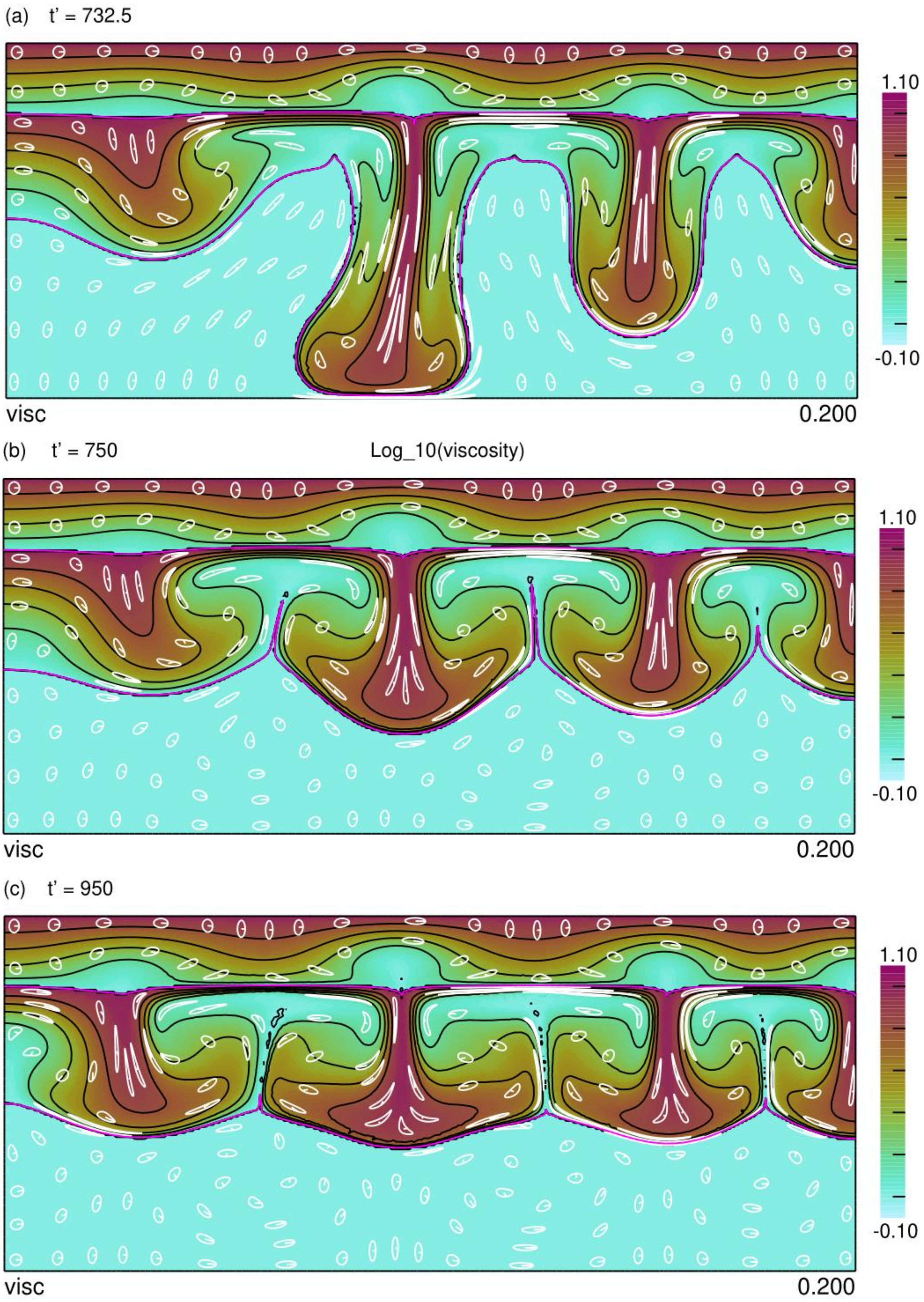

Figure 4. With format as in Fig. 3, these maps show 2D sections of the viscosity after the instability has developed for calculations in which *a* = -0.5, *t'* = 732.5 (*t* = 18.3 Myr) (a), *a* = -1, *t'* = 750 (*t* =

18.8 Myr) (b) and $a = -1.5$, $t' = 950$ ($t = 23.8$ Myr) (c), with dimensional times quoted for $\eta_0 = 10^{20}$ Pa s. In (a) the upper half of the mantle lithosphere is denser than the asthenosphere and is enabled to punch through the asthenosphere. In (b) and (c) the intrinsic buoyancy of the mantle lithosphere is sufficient to contain the circulation within the mantle lithosphere, though in both cases there are large disturbances to LAB topography and upward entrainment of minor amounts of asthenospheric material.

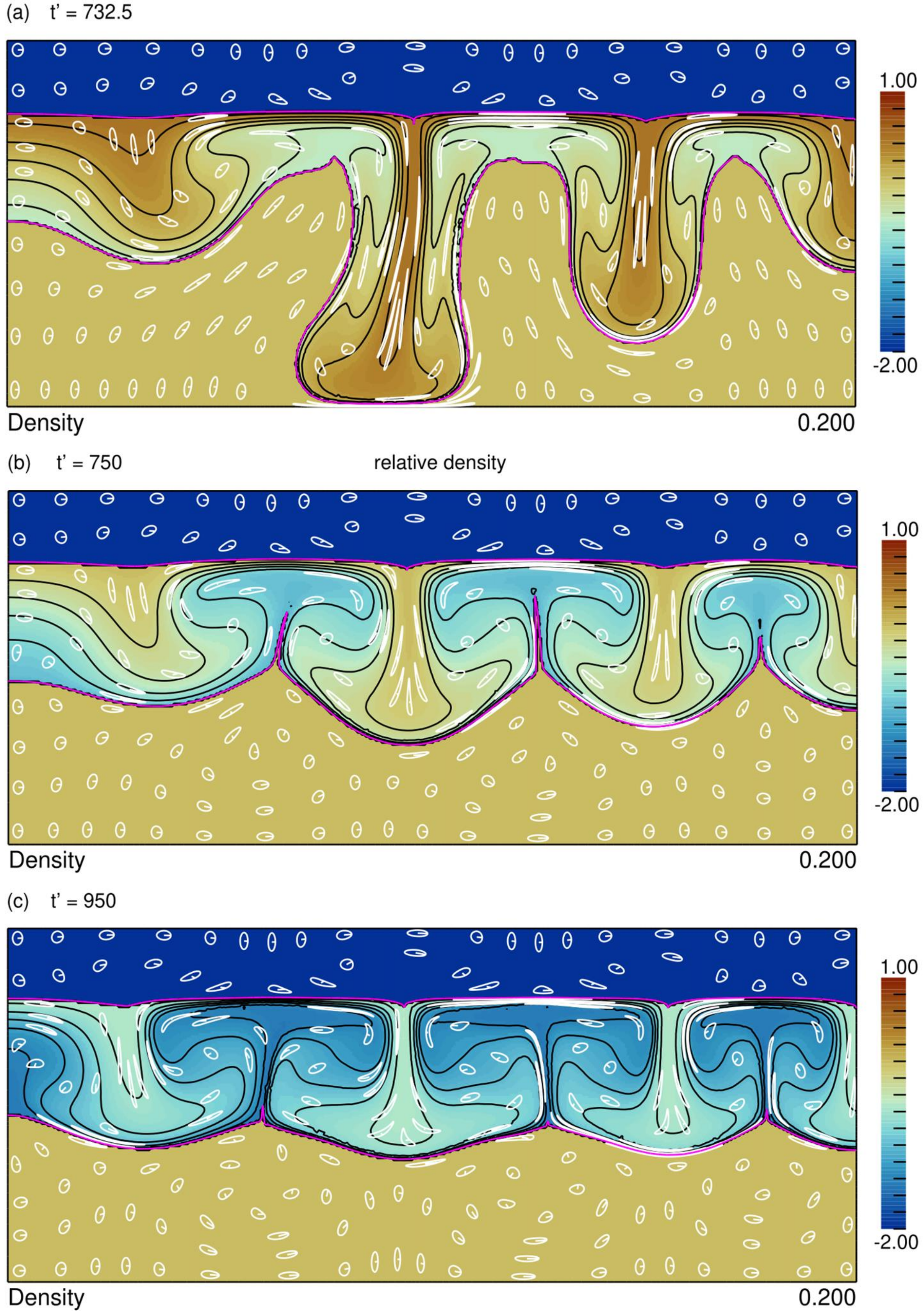

Figure 5. For the same three calculations in Fig. 4, these maps show 2D sections of the relative density variation after development of the instability with a = -0.5, t' = 732.5 (t = 18.3 Myr) (a), a = -1, t' = 750 (t = 18.8 Myr) (b) and a = -1.5, t' = 950 (t = 23.8 Myr) (c), with dimensional times quoted for $\eta_0 = 10^{20}$ Pa s. The reference value ($\rho' = 0$) for the relative density is that of the

asthenosphere, and the relative density within the mantle lithosphere varies from $\rho' = a$ to $1 + a$. The relative density in the crust is off-scale at $\rho' = -7.88$.

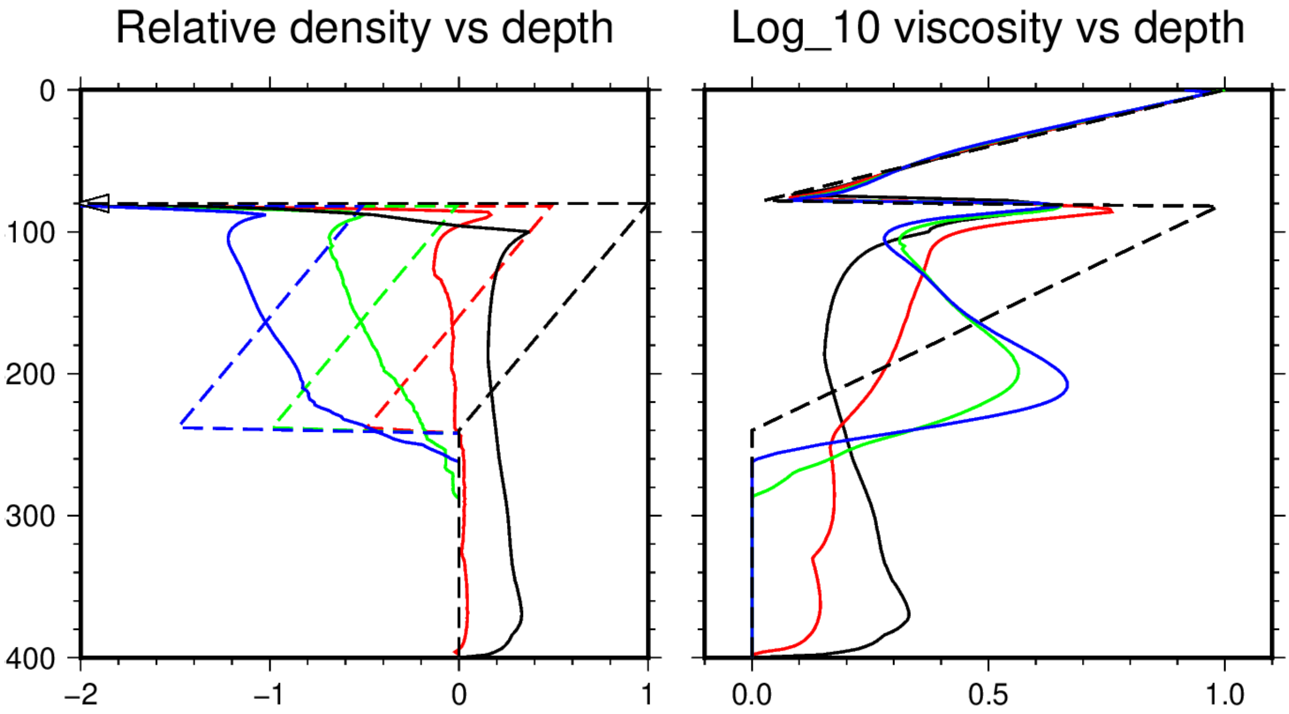

Figure 6. Depth profiles of horizontally averaged relative density (left) and viscosity (right) for the 4 cases illustrated in Figs. 3-5: $a = 0$ (black), $a = -0.5$ (red), -1.0 (green), -1.5 (blue). The dashed lines are those that apply at $t' = 0$, the solid lines apply at the same times shown in Figs. 3-5. The viscosity profiles at $t' = 0$ are the same in all cases. A geometric average is shown for viscosity, that is the lateral average of $\log_{10}(\eta')$ as shown in Figs. 3-5.

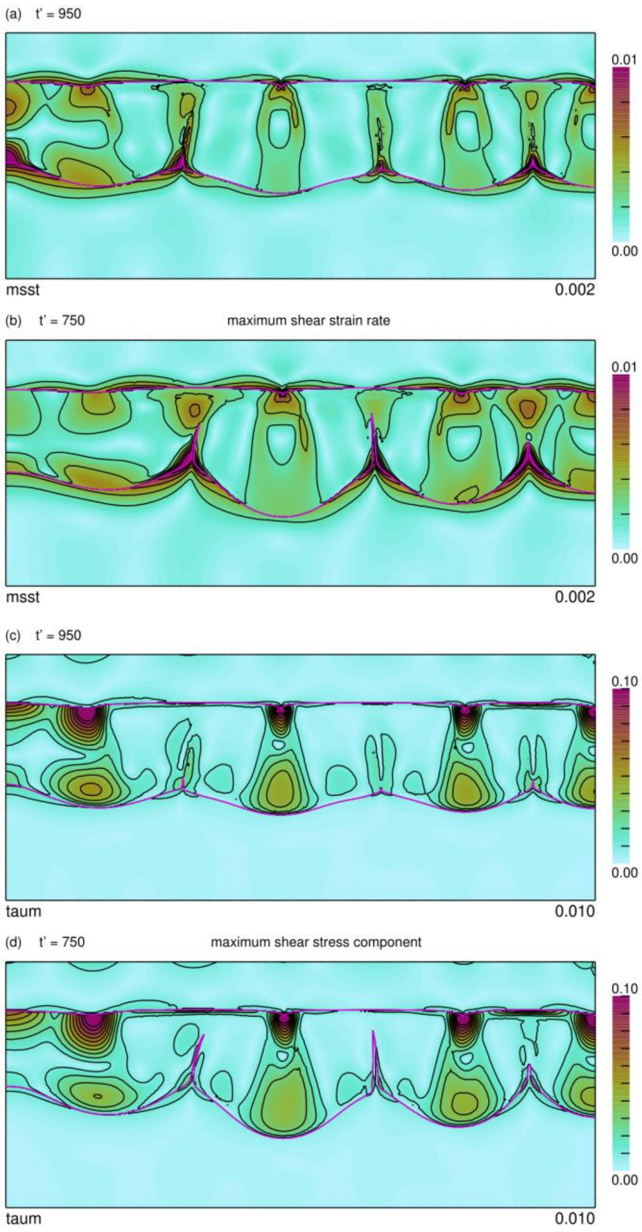

Figure 7. For *a* = -1.5 (a,c) and *a* = -1.0 (b,d) at the same times shown in Figs. 4,5 (a) and (b) show contours of the maximum shear strain rate component, (c) and (d) show contours of maximum shear stress component. Contours are labelled in dimensionless units and may be scaled using the scale-factors $gL\Delta\rho_T/\eta_0$ and $gL\Delta\rho_T$ for strain rate and stress respectively (nominally 40.4 per Myr and 128 MPa respectively for $\eta_0 = 10^{20}$ Pa s). The interfaces that represent the model Moho and the model LAB are shown by a magenta line. The colour map is allowed to saturate in places in order to better show some of the second order structure in the solution.

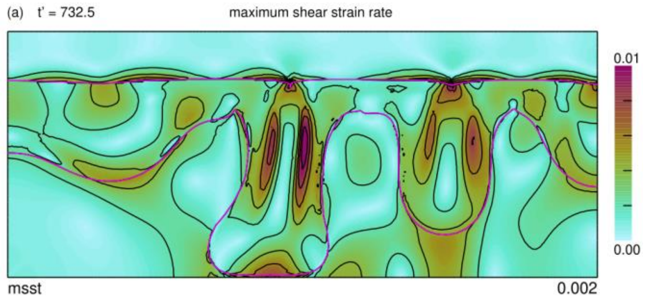

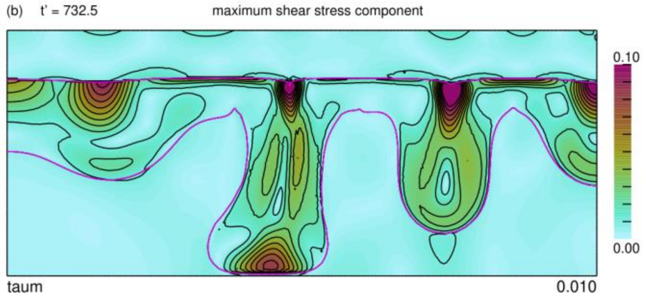

Figure 8. For *a* = -0.5 at the time as Figs. 4,5a, (a) shows contours of the maximum shear strain rate component, (b) shows contours of maximum shear stress component. Contours are labelled in dimensionless units and may be scaled using the scale-factors $gL\Delta\rho_T/\eta_0$ and $gL\Delta\rho_T$ for strain rate and stress respectively (nominally 40.4 per Myr and 128 MPa respectively for $\eta_0 = 10^{20}$ Pa s). The interfaces that represent the original *cr/ml* interface and *ml/as* interface are shown by a magenta line.

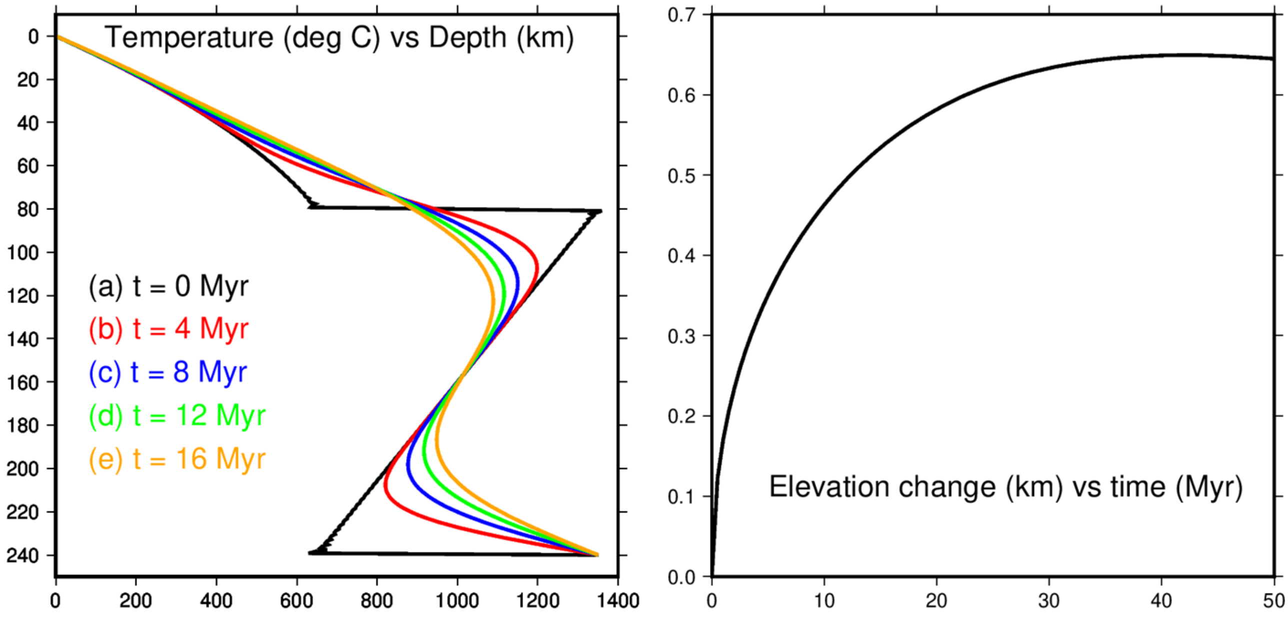

Figure 9. Laterally averaged geothermal profile (left) for the simplified case in which the buoyant mantle lithosphere layer is overturned at time zero (black line) and then re-equilibrates by thermal diffusion. During the re-equilibration heat enters the base of the lithosphere from the asthenosphere beneath and flows into the crust from the top of the lithosphere, so there is a net heating of the layer in the depicted time interval. The net heating causes the upper surface to rise (right) if isostasy prevails. On the time-scale of about 500 Myr the thermal transient decays and the pre-overturn geotherm (Fig. 2) is restored.

Highlights

❿ The mantle lithosphere beneath Tibet has undergone gravitational instability causing magmatism

❿ Tomographic images show that the mantle lithosphere beneath Tibet remains in place

❿ Internal overturn of the mantle lithosphere layer can explain both tomography and magmatism

Gravitational Instability of Thickened yet Compositionally Buoyant Tibetan Mantle Lithosphere

Gregory A. Houseman
School of Geophysics and Information Technology, China Univ. of Geosciences, Beijing, China;
and School of Earth and Environment, University of Leeds, Leeds, LS2 9JT, UK

Philip C. England
Department of Earth Sciences, Oxford University, S Parks Rd, Oxford, OX1 3AN, UK

Lynn A. Evans
School of Earth, Atmosphere and Environment, Monash University, Clayton, VIC, Australia

Abstract

The Tibetan plateau, one of the major topographic features of the Earth, presents many unanswered questions regarding its evolution, present structure, and continuing geological activity. The extensive crustal thickening that is attributed to continental convergence between India and Eurasia sustained for the past 55 Myr, and continuing today, is underlain by an upper mantle in which relatively fast shear-wave speeds are measured to depths of 200 km and more. Although the high elevation of the plateau can be attributed mainly to the thickness of the crust, the observation that the plateau is now extending is evidence that the lithosphere has increased its gravitational potential energy since it was thickened. Extensive volcanism during the current continental collision, additionally implies that the lithosphere and/or uppermost mantle of Tibet was re-heated. Replacement of mantle lithosphere by asthenosphere in a convective thinning process has been advanced as an explanation of that re-heating, but that process has been difficult to reconcile with the high shear-wave velocities measured in the upper mantle beneath the plateau. However, a model based on a restricted overturn of a depleted, metasomatised, mantle lithosphere in the upper 200 km of the mantle can reconcile these apparently contradictory observations. Such overturn can explain how the observed distribution of seismic velocities has been produced, how heat is injected into the lithosphere producing transient uplift, and how mantle-derived melts can rapidly reach the base of the crust in widely distributed locations across the plateau.

Introduction

The crustal thickness of the Tibetan Plateau varies between about 60 and 75 km (Nábelek et al., 2009; Kind and Yuan, 2010; Yuan et al., 1997; Zhang et al., 2011; Gao et al., 2013; Shen et al., 2016), in contrast with normal continental crustal thickness of 35 to 40 km. The Tibetan crust has been thickened by the continuing continental collision of India and Eurasia since at least 55 Ma (Yin and Harrison, 2000; Garzanti, 2008). Thrust faulting, often associated with older suture zones, enabled crustal thickening (Yin and Harrison, 2000). Throughout this period, large-scale lateral displacements have been mediated by a combination of continuous deformation and displacements on strike-slip fault systems (England and Molnar, 2005; Tapponnier and Molnar, 1977; Fang et al., 2024). A combination of strike-slip and thrust deformation continues to govern deformation on the margins of the plateau (Burchfiel et al., 2008; Ou et al., 2022). However, since about 10-15 Ma, the onset of rifting on a set of north-south structures (Armijo et al., 1986; Styron et al., 2013) indicates that most of the plateau has been extending in the E-W direction (Gan et al., 2021) faster than it shortens in the N-S direction. From current geodetic dilatation rates, the crust of the plateau is estimated to have thinned by more than 5 km during this period (Ge et al., 2015). Although some authors, beginning with Argand (1924) have argued for the concept of Tibet being raised by the under-thrusting of a rigid “Greater India” plate that extends 1000 km or more across the plateau, we assume for the purpose of these calculations that the Tibetan lithosphere in general has remained vertically coherent as it has been shortened, thickened and sheared during the India-Asia collision.

England and Houseman (1989) argued that the mechanism which would most simply explain the change in the tectonic environment of the plateau, from convergence and thickening to extension and thinning, involved the removal of relatively dense, colder, mantle lithosphere from beneath the plateau, and its replacement by hot asthenosphere. They suggested, following Houseman et al. (1981), that this could be accomplished simply by a convective destabilisation of the viscous upper mantle. In mechanical terms, heating or replacement of relatively cold lithosphere causes an elevation increase under isostasy, so that the vertical compressive stress component can increase to the point where it is greater than one of the principal horizontal compressive stress components. The re-orientation of the principal stresses can then cause east-west extension rates to exceed north-south shortening rates, allowing the onset of normal faulting alongside persistent strike-slip shear. The arguments in favour of a convective thinning event beneath Tibet at around 10-15 Ma seemed robust until studies based on the propagation of seismic surface waves showed that a layer of cold, relatively fast, mantle remains in place beneath much of the Tibetan Plateau at depths of around 200 km (Huang et al., 2003; Priestley et al., 2006).

A simplified tectonic map of the Tibetan Plateau (Fig. 1) shows the major suture zones separating Lhasa, Qiangtang and Songpan-Ganze terranes progressively coalesced by pre-collision ocean closure, and subsequently shortened by North-South convergence (Yin and Harrison, 2000). Fig. 1 also shows locations of normal faults delineating rifts developed in the south of the plateau as a consequence of East-West extension dating from the mid-Miocene. An important indication of the process that changed the tectonic environment of Tibet follows from the widespread post-collision volcanism affecting most parts of the Tibetan Plateau (Fig. 1; Chung et al., 2005; Ding et al., 2003). In particular, potassic to ultrapotassic volcanic rocks in the Qiangtang terrane (~45-29 Ma), the central and western Lhasa terrane (~25-8 Ma) and the Songpan-Ganzi terrane (~17-1 Ma) are interpreted to have been derived from metasomatised mantle sources which may have undergone distinct and complex enrichment histories (Chung et al., 2005; Ding et al., 2003). The relatively high potassium content of these magmas indicates a K-rich phase like phlogopite in the source region, interpreted as representing enriched sub-continental mantle lithosphere. The age of the enrichment is debated, with Ding et al. (2003) suggesting that it could be attributed to different phases of Mesozoic and Cenozoic subduction on the major suture zones that separate Lhasa, Qiangtang and Songpan-Ganzi terranes, whereas Turner et al. (1996) inferred Proterozoic or even Archaean age for the metasomatism based on radiogenic isotope ratios. In general the potassic lavas are associated with late Cenozoic rift systems that are diagnostic of the onset of east-west extension in the plateau, and the spatial and temporal correlations imply that the potassic magmatism and the lithospheric extension are symptoms of the same process. Based on thermal arguments, Turner et al. (1993) concluded that the only plausible means to attain temperatures high enough for melting within the lithospheric mantle beneath Tibet was a widespread convective thinning event affecting most of Tibet. Chung et al. (2005) interpreted distinct thinning events affecting the lithosphere under the different terranes. Consistent with the idea of multiple events, Ding et al. (2003) pointed out that melting related to subduction at the thrust systems on the terrane boundaries seemed to explain why magmatic belts with distinctive source signatures are aligned with the major terrane boundaries.

Whether the mantle lithosphere beneath Tibet has been thinned or not is thus a central question in the interpretation of both tectonic and magmatic evolution of the Tibetan lithosphere. Measurement of shear velocity versus depth obtained from tomographic analysis of surface waves provides a key constraint on the question. Priestley et al. (2006) used this method to map the base of the East Asian lithosphere, concluding that the Tibetan lithosphere remains in place, and in fact that the lithosphere beneath Tibet is similar to tectonically stable Archaean and Proterozoic cratons which may attain a thickness of more than 250 km (Artemieva and Mooney, 2001). Velocity-depth profiles obtained from surface-wave analysis are not in question, but caution is required with the interpretation because averaging of velocity with distance along the path travelled by the seismic waves must be taken into account. The ability to resolve lateral changes in velocity also decreases with depth because, at deeper levels velocity is only constrained by surface waves of greater wavelength. Horizontal velocity variations on distances that are less than some small multiple of the seismic wavelength are simply not measurable using surface waves. Tomographic inversion tends to introduce further smoothing of the velocity field because the tomographic problem is intrinsically under-constrained.

In considering how to reconcile these different data and different interpretations of how the Tibetan lithosphere has been affected by the continental collision, we here revisit the convective thinning hypothesis proposed by Houseman et al. (1981) and England and Houseman (1989), but we amend one of their basic assumptions: we here allow for an intrinsic density difference between the sub-continental mantle lithosphere and the asthenosphere beneath. Jordan (1978) proposed that cratonic lithosphere must be stabilised against convective overturn in order to enable the long-term stability of these zones of thickened lithosphere in a concept termed the *isopycnic tectosphere*. He inferred the likely stabilisation mechanism to be density reduction caused by extraction of basalt melts. Based on xenolith analyses from a global catalogue, Poudjom Djomani et al. (2001) demonstrated that the density of depleted mantle lithosphere is intrinsically less than that of primitive upper mantle (McDonough and Sun, 1995), and moreover, that the density deficit increases with the tectonic age of the craton. Archaean-age cratons have mantle lithosphere with the most depleted (and most buoyant) signature. More recently active cratons may have been re-fertilized by metasomatism, causing a reduction in buoyancy, but Griffin et al. (2009) conclude that most Proterozoic-age cratons remain buoyant relative to primitive upper mantle. Kay and Mahlberg-Kay (1993) considered the impact of intrinsic buoyancy resisting or slowing delamination, but concluded that there is anyway extensive evidence for magmatism produced by delamination. In any case, a positively buoyant layer of mantle lithosphere might still be subject to gravitational instability even if it is not removed.

Because the density of Tibetan mantle lithosphere is not well constrained, we here compare calculations that simulate a gravitational instability developed within a mantle lithosphere layer which has an intrinsically lower density. We consider experiments with differing amounts of compositional buoyancy, and show that a positively buoyant layer of mantle lithosphere may remain in place, while undergoing comprehensive overturn. Using simplified numerical experiments which illustrate the process, we argue that the process is : (a) likely to have occurred beneath Tibet, given what we know of the relevant physical properties, (b) able to explain recent thermal rejuvenation and volcanism of the plateau without requiring the loss of lithospheric mantle beneath the plateau, (c) consistent with seismic velocity structure of the lithosphere in Tibet and surrounding regions, and (d) consistent with localised melting of mantle lithosphere, basaltic volcanism, and a rapid heating of the lower crust by plutonism.

Numerical Experiments

We consider a simplified two-dimensional system consisting of three layers of incompressible viscous fluid: crust (*cr*), above mantle lithosphere (*ml*), above asthenosphere (*as*). We want to investigate the case in which the middle layer is unstable due to a temperature-induced internal stratification of density decreasing with depth. The process that we describe below is essentially a Rayleigh-Taylor instability of the middle layer; for simplicity we neglect thermal diffusion in these experiments. Although doing so means that the instability may develop faster than the case where diffusion is included, the difference will be small because the time scale of interest (10 to 20 Myr) is small compared to the thermal time constant of the layer. The properties of the fluid (density and viscosity) are transported by the flow and we continuously track the internal distribution of density and viscosity as the instability develops. The two material interfaces representing the Lithosphere-Asthenosphere boundary (LAB) and the Moho are especially significant. Our aim here is to examine the consequences of the overturn of the mantle lithosphere and whether the process is consistent with geophysical and geochemical data from the Tibetan Plateau. We assume as a plausible example that the mantle lithosphere layer has a thickness L (nominally 160 km), the overlying crust has thickness $L/2$ and the thickness of asthenosphere above the transition zone is also L. Thus the model Moho is initially a uniform 80 km deep and the model LAB is 240 km deep.

We assume that this model starting condition has been produced by sustained convergence in the collision zone causing shortening and thickening of the lithospheric layers. To simplify, we assume the initial geotherm varies linearly with depth in the mantle lithosphere and is constant in the asthenosphere beneath. If the temperature at the LAB is nominally 1350°C and that at the Moho is 650°C (Fig. 2), the density difference between bottom and top of the middle layer $\Delta\rho_T$is a consequence of thermal expansion acting on a temperature contrast of order 700°C. For a thermal expansion coefficient of 3.5 x 10^{-5} K^{-1} (Bouhifd et al., 1996), the density increases from the LAB to the Moho by$\Delta\rho_T \approx 80 \mathrm{kg\ m}^{-3}$.

The lower layer representing asthenosphere is assumed to have a constant temperature and density but we allow for an intrinsic density difference between mantle lithosphere and asthenosphere attributed to geochemical depletion and represented by a step change in the initial density profile at the LAB: $\Delta\rho_C = \rho_{as} - \rho_{mlab}$. Based on the compilation of Griffin et al. (2009), $\Delta\rho_C$= 78 kg/m^3 is a representative estimate for the average reduction in density of mantle lithosphere of Archaean age relative to primitive upper mantle. This density contrast decreases to 40 kg/m^3 for mantle lithosphere of Proterozoic age, but Griffin et al. (2009) infer that the earliest Archean lithosphere was even more depleted and less dense. In the following calculations we consider a non-dimensional relative density profile scaled by $\Delta\rho_T$ (Fig. 2), such that $\rho'_{as} = 0$ in the lower layer, ρ'_{ml} varies linearly from $a = -\Delta\rho_C/\Delta\rho_T$ at the base of the mantle lithosphere ($z = L+h$) to $1+a$ at the top of the mantle lithosphere ($z = h$), and $\rho'_{cr} = (\rho_{cr} - \rho_{as})/\Delta\rho_T \approx -7.88$in the crustal layer. We ignore variation of density within the crustal layer. Given the uncertainty in both thermal and intrinsic density contrasts, we treat the parameter a (the ratio of compositional to thermal density contrast between asthenosphere and mantle lithosphere layers) as a free parameter, and consider here values of $a = -1.5, -1,$and $- 0.5$(Fig. 2).

In these numerical experiments we assume a linear dependence of strain rate on deviatoric stress, but allow the viscosity coefficient to vary with position, and assume that the physical properties (density and viscosity) are advected by flow within the system of layers. The initial distribution of viscosity in the 3-layer system is based on an exponential decrease of viscosity with depth in both crust and mantle lithosphere layers. In each case we assume a factor of 10 decrease from top of the layer to base of the layer. The viscosity at the base of the crust is set to η_0, the same value as the viscosity at the base of the mantle lithosphere, and the same as the uniform viscosity assumed for the asthenosphere. Although aspects of the viscosity profile used here (Fig. 2) are ad hoc, and further experiments with different possible viscosity profiles may be called for, it is consistent with the idea of viscosity decreasing systematically with depth in both crust and mantle lithosphere, with lowermost crust being significantly weaker than uppermost mantle, and with the asthenosphere being relatively weak compared to uppermost mantle. The main effect of increasing the viscosity at any level in the model is to increase the time required for an instability to develop. In our calculations, viscosity is rendered dimensionless by η_0, distance by L, relative density by $\Delta\rho_T$, stress by $gL\Delta\rho_T$, time by $\eta_0/(gL\Delta\rho_T)$, and velocity by $(gL^2\Delta\rho_T)/\eta_0$. Thus, if $\eta_0 = 10^{20}$ Pa s, the time scale-factor is 0.025 Myr and the velocity scale factor is 6.45 m/yr.

We model a 2D region whose width is 6 times the thickness of the mantle lithosphere L (nominally 960 km). We assume the vertical side walls of the 2D region are reflecting boundaries, with zero vertical traction and zero horizontal velocity. We also set the upper and lower horizontal boundaries to zero horizontal traction and zero vertical velocity. We introduce a small perturbation to both density and viscosity fields from which instability can grow. This perturbation is ad hoc, but includes harmonic components of wavelength $12/n$, with integer $n = 1,2,3 \ldots 8$. We thus allow the instability to favour the fastest growing wavelength for Rayleigh-Taylor instability from among the different components of the perturbation. Typically, the fastest growing instability has a wavelength about 3 times the unstable layer thickness; the other components of the perturbation also introduce some irregularity to the solution, but do not have a strong effect on the time required for the instability to develop.

The instability is allowed to develop by time-stepping, with the density and viscosity fields advected by the flow field computed at each time level. At each time-level, we balance stress gradients (pressure p, and deviatoric stress τ_{ij}) against body force (g_i), assuming inertial terms are negligible

$$\frac{\partial\tau_{ij}}{\partial x_j} + \frac{\partial p}{\partial x_i} + \rho g_i = 0, \tag{1}$$

and the plane-strain flow is incompressible:

$$\frac{\partial u_i}{\partial x_i} = 0 \tag{2}$$

for velocity components u_i, and rates of strain governed by a Newtonian viscosity law with spatially variable viscosity:

$$\tau_{ij} = \eta(x, y)\left(\frac{\partial u_i}{\partial x_j} + \frac{\partial u_j}{\partial x_i}\right) \tag{3}$$

The algorithm is implemented in the program *basil* (Houseman et al., 2008; Fang et al., 2024). The solver for the velocity field uses the finite element method applied on an irregular mesh of triangles using 6-node quadratic interpolation functions for velocity components and 3-node linear interpolation for pressure. The pressure discontinuity that is implied where there is a discontinuity of viscosity (e.g., across the Moho) is handled by duplicating the nodes on that boundary and adding another set of constraints to enforce continuity of velocity at those node pairs. The finite element mesh is advected with the flow, and when the mesh is sufficiently distorted, a new mesh is created respecting the current domain interfaces, and the current density and viscosity fields are interpolated on to the updated mesh. We track internal strain within the 2D flow field by advecting a set of initially circular markers that are deformed by the shear flow as they are translated.

The flow field that develops in the presence of this initial density distribution is dependent of course on the variation of viscosity η within the layers. Although there is no motive force for flow within the upper and lower layers owing to their initial uniform density, the developing instability in the middle layer necessarily induces flow in the layers above and below, due to variations of normal and shear stress developed on the interfaces. Deflections of the internal interfaces develop under the influence of the forces produced by the lateral density gradients as the gravitational instability develops. We neglect the impact of thermal diffusion in these calculations, based on the simplifying assumption that growth of the instability is rapid compared to the time scale for significant thermal diffusion to occur.

Results

The convective overturn that arises as a consequence of the experimental set-up is illustrated in Fig. 3 for a case where $a = 0$ (no compositional buoyancy) and sufficient time has elapsed for the initial instability to approach completion. This experiment illustrates the convective thinning of most of the mantle lithosphere in a period of about 10 Myr in a manner that is consistent with the convective thinning process described by Houseman et al. (1981). In these experiments we imposed a boundary at 400 km depth in order that the flow process occurring in the uppermost mantle can be better resolved, but it is expected that in reality any downward flow that reaches the upper mantle discontinuity at 410 km would likely continue sinking into the transition zone. The experiment shown in Fig. 3 has high viscosity (η' = 10) and high density ($\Delta\rho' = 1$) at the top of the mantle lithospheric layer, but much of the high viscosity material near the top of the layer is effectively removed by the instability. The relatively low viscosity of the lowermost crust is significant in enabling the high viscosity upper mantle to move laterally and, as it does so, to drag lower crust into a pile that pushes the Moho down and the Earth's surface upward, causing extensional strain in the upper crust above the loci of mantle downwelling. Between the downward push of thickened crust and pull of heavy mantle lithosphere, significant downward deflection of the Moho occurs.

In Figs. 4 and 5 we show the corresponding instability that develops for the three cases in which non-zero compositional buoyancy is assumed with a = -0.5, -1.0 or -1.5 for the initial density profiles illustrated in Fig. 2. In each of these experiments we used the same initial viscosity distribution and the same initial perturbation used in Fig. 3. For a = -1 or -1.5, the intrinsic density contrast between mantle lithosphere and asthenosphere is sufficient to preserve the separate layering, though relatively large displacements of the LAB interface occur as the instability develops, and minor entrainment of the asthenosphere through the mantle lithosphere can occur. When$a = -0.5$, a large fraction of the mantle lithosphere can penetrate the asthenosphere layer and sink to the transition zone, although the lower half of the *ml* layer is buoyant relative to the asthenosphere and resists entrainment. Comparing the case of a = -0.5 (Fig. 4a,5a) to that of a = 0 (Fig. 3), the instability takes almost twice as long and the final dominant wavelength is between about λ' = 1.5 and 2, rather than λ' = 3. The dominant wavelength for a = -1 or a = -1.5 is also between about λ' = 1.5 and 2. The selection of dominant wavelength reflects whether the circulation is restricted to the thinner *ml* layer by positive buoyancy, or involves both *ml* and *as* layers (effectively twice the thickness). We also considered the possibility that the instability with $a = -1$ might be able to develop at longer wavelengths, by repeating our experiment with short wavelength components of the initial perturbation removed, leaving harmonic perturbations that explicitly included wavelengths only of λ' = 6 and 12. We found that the instability developed more slowly and, even though the shorter wavelength perturbation was not present in the initial state, a secondary instability at the shorter wavelength developed (presumably from rounding noise). These tests imply that in the presence of a random perturbation that includes a broad range of harmonics, the instability in a positively buoyant layer will develop at a wavelength between 1.5 and 2 times the unstable layer thickness.

The thinning of the uppermost dense part of the mantle lithosphere between the downwelling sheets appears similar in all of these experiments. The residual parts of this layer have undergone extreme thinning by lateral stretching, as indicated by the horizontal elongation of the originally circular strain markers. Material that originated in the lower part of the mantle lithosphere is juxtaposed against this residual layer, bringing high temperatures close to the base of the crust. For $a = 0$ (Fig. 3) this hot material was originally asthenosphere, whereas for$a = -0.5$(Fig. 4,5) the asthenosphere is buffered by a considerable thickness (of order 50 km) of basal lithosphere that was relatively buoyant, and still relatively hot. Laterally averaged profiles of the density and viscosity (Fig. 6) provide another perspective on the redistribution of material in the *ml* layer. For a = -1 and -1.5, we see that the density vs depth profile within the *ml* layer is effectively inverted, leaving a relatively thin boundary layer of residual material at the top of the layer, and a more diffuse gradient at the base of the layer, related to the depth variation of the interface between *ml* and *as* layers after the instability has developed.

While the model LAB is completely disrupted in those experiments with $a = 0$ and $a = -0.5$, it is preserved in a very perturbed state with $a = -1$ and $a = -1.5$. Strong lateral gradients in the depth to the *ml/as* interface are possible when the asthenosphere density is close to the density of the material that was stripped from the uppermost mantle and ends up pooling near the base of the mantle lithosphere (Fig. 4,5b,c). With $a = -1.5$, there remains a significant density contrast across the LAB interface and its depth variation is smaller by about a factor of 2, though still in the range240 ± 20km(Fig. 4,5c). In both of these experiments, the strain markers show that the flow velocity is approximately parallel to the material interface and the up-slope flow of the overturning layer is shearing and dragging asthenosphere toward the shallowest part of the *as* layer beneath an upwelling material flow in the *ml* layer. While the resolution of the numerical experiments makes it difficult to quantify amounts and rates, it seems likely that this flow field would inject minor amounts of asthenospheric material into the upwelling flow in the *ml* layer, and rapidly transport it to the upper part of the *ml* layer.

The density contrast across the *cr*/*ml* interface is so much larger than that across the *ml/as* interface, that the deflection of the model Moho is much less than the deflection of the model LAB. Nonetheless, significant deflections of the Moho are represented in these models. The upward deflection of the Moho is of order 1.5 to 3 km over the extensive areas of upwelling, whereas localized downward cusps are deflected as much as 10 km beneath piles of hot lower crustal material that are swept into the sites above downwelling in the *ml* layer. The Moho deflection amplitudes are similar in the three experiments shown in Figs. 4,5 because in each case, the quantities of dense material in the sinking structures of the *ml* layer are similar. The variation in the normal stress on the upper surface of the model, which amounts to about 5 MPa (peak to peak) in each of these experiments, can be interpreted as a variation in the vertical deflection of the surface of order 200 m, with relative uplift occurring over areas where the crust is thickened. In Fig. 3 the greater dominant wavelength results in more material being entrained in each of the more widely-spaced downwellings and thus in greater deflection of the model Moho as the instability develops.

It is also notable that the extent to which the crustal layer is perturbed by the instability is similar in all three experiments shown in Figs. 4,5. The response of the crust to the thinning and downward transport of the uppermost *ml* layer is here dependent on the assumed low viscosity of the basal *cr* layer, but we found that whether the lower *cr* layer is weak or strong does not have a strong impact on the overturn of the *ml* layer.

Maps of the maximum shear strain rate and the maximum shear stress (Fig. 7 and Fig. 8) reveal other important aspects of how the instability develops. The two cases in which the instability is contained within the original *ml* layer are similar in showing that maximum shear strain rates (Fig. 7, left) are greatest (of order 1% per Myr) near the *ml/as* interface, especially near the convergent flow beneath the upwelling within the *ml* layer. The strain rate maps are evidently consistent with the extreme deformation indicated by the strain-markers in Figs. 4,5. High strain rates are also evident in the basal layer of the crust, where low-viscosity material is dragged along by higher viscosity material in the upper part of the *ml* layer. In contrast the maximum shear stress maps (Fig. 7, right), which are basically obtained as the product of maximum shear strain rate and local viscosity, present a different perspective. The stress-difference maps are dominated by high-stress (of order 20 MPa) regions where the upper high-viscosity part of the *ml* layer is pulling away from the Moho. Song and Klemperer (2024) have described clusters of sub-Moho earthquakes in west Tibet and beneath the High Himalaya in south Tibet, which they interpret as caused by drips of eclogite. The model presented here provides a possible explanation for such observations that does not require eclogite to drive the flow. The distribution of sub-Moho seismicity beneath Tibet would be diagnostic of differential deformation within the mantle lithosphere layer, but it is unclear whether mantle seismicity beneath other parts of Tibet is yet adequately known to provide a useful constraint. For a = -0.5 (Fig. 8) in which the flow is not contained within the *ml* layer, the dominance of the stresses at the separation point of downwelling and Moho is similar to that of Fig. 7, and high strain rates are again observed in the lower crust, but the maximum strain rates beneath the Moho now occur on the sides of the downwelling sheets where relatively buoyant material either side of the downwelling is resisting the downward drag of the dense material in the core of the structure.

Discussion

The concept of continental lithosphere being de-stabilised and removed by a process of delamination, convective thinning, or mantle drips has been explored by many authors in the past five decades, in the context of regions including the Colorado Plateau (Bird, 1979; Levander et al., 2011), Tibet (Houseman et al., 1981; England and Houseman, 1989; Molnar et al., 1993; Houseman and Molnar, 1996; Turner et al., 1996), South America (Garzione et al., 2006; Kay and Mahlburg-Kay, 1993; Andersen et al., 2022), the Sierra Nevada (Saleeby and Foster, 2004), Iran (e.g. Hatzfeld and Molnar, 2010; Zarunizadeh et al., 2024), the Anatolian Plateau (Göğüş et al., 2017), the Carpathians, (Lorinczi and Houseman, 2009), New Zealand (Stern et al., 2013), and the North China craton (Gao et al., 2002). At least in the Carpathian case (and probably elsewhere) it seems clear from seismic tomography that material removed from the lithosphere can reach and pond in the mantle transition zone (Dando et al., 2011; Ren et al., 2012).

Tibet seems to be an exceptional case; the seismic tomography suggests that most of the lithosphere has remained in place (Priestley et al., 2006) while magmatism implies that some form of gravitational instability in the upper mantle has occurred. We argue that this is most simply explained by the mantle lithosphere here having a compositional density deficit relative to the asthenosphere. We have sketched here the basic mechanical process of instability occurring within a layer of depleted mantle lithosphere. If there is sufficient intrinsic buoyancy, the mechanism described here permits the depleted layer to remain in place after overturn. The overturn of the layer moves hot material from near the base of the lithosphere, to near the base of the crust. As the hot mantle lithosphere rises, decompression melting can occur to produce mantle melts such as alkaline basalts; as the lower crust heats by conduction, plutonism producing more silicic melts is likely.

The time scale on which the overturn instability proceeds (Figs. 3-5) is proportional to the viscosity scale constant η_0. We do not consider this viscosity to be well constrained a priori, but it is apparent from these calculations that a value greater than about 10^{20} Pa s would slow the overturn so much that it would not proceed fast enough to explain what has happened in Tibet during the last 20 Myr or so. Although the intrinsic density of the Tibetan mantle lithosphere is also not well constrained by seismic velocity measurements, seismic tomography images based on surface wave analysis appear to show that the mantle lithosphere remains in place beneath Tibet, while the tectonic, volcanic and magmatic history imply that there has been a significant transfer of heat into the lithosphere. The simplest way to reconcile these observations is to conclude that the mantle lithosphere has experienced a gravitational instability, but has not sunk in to the underlying asthenosphere because of its compositional buoyancy. Although both density and viscosity values inferred here for the Tibetan mantle lithosphere layer are low compared to values estimated in other continental environments, these low values follow as a logical deduction if we accept the evidence that an in situ mantle overturn has occurred.

This type of mantle instability could easily be slowed to the point of irrelevance by the relatively high viscosities that are thought to characterise other thick continental cratons (Artemieva, 2011; Pearson et al., 2021), so why is this process more in evidence beneath Tibet ?

Two factors may be important: firstly, the externally imposed convergence of this region has maintained relatively high strain rates overs 10's of millions of years since the collision began. These large strain rates effectively decrease the viscosity of all lithospheric layers when power-law viscosity or high-temperature plasticity mechanisms become active, because of the non-linearity of the applicable rheological laws (Hirth and Kohlstedt, 2013). Secondly, the rate of growth of Rayleigh-Taylor instability increases directly in proportion to the thickness of the unstable layer (Conrad and Molnar, 1997); as the lithosphere thickened during the collision it became increasingly likely that the mantle lithosphere would overturn.

Although the experiments described here represent an instability in two dimensions, the development of Rayleigh-Taylor instability in three dimensions has the same initial growth rate for $k^2 = k_x^2 + k_y^2$ regardless of the relative contributions of k_x and k_y (the x and y wavenumber components of a harmonic perturbation that develops into a flow field). A random initial perturbation of the density structure in the Tibetan mantle lithosphere would result in a 3D instability developing (Kaus and Podladchikov, 2001), with multiple localized downwelling sites separating a greatly thinned mantle lid. However, these 2D simulations provide a reasonable guide to the behaviour of a 3D flow, including the time scale on which the instability develops, the typical horizontal separation of the vertical thermal structures, and the overall inversion of the average density and thermal structure caused by the overturn (Fig. 6). It seems unlikely that a mantle lithosphere instability affected the whole plateau at the same time. Chung et al. (2005) describe spatial and temporal variations in the magmatic activity that has impacted different parts of the plateau at different times. Such variations may be expected to arise from the natural variability of material properties and the tectonic structures developed when the major terranes were assembled and underwent collisional orogeny. Based on the compilation of Chung et al. (2005), one would infer that the Qiangtang and W. Yangtze were first affected by extensive magmatism in the Eocene and Oligocene, the Lhasa terrane during the Miocene, and the Songpan-Ganze and W. Qiantang since the mid-Miocene and into the Quaternary. Xia et al. (2023) also describe major variations in lithospheric thermal structure across the Plateau based on a synthesis of regional geophysical data, and identify the north-central Qiangtang and central Songpan-Ganzi Blocks as having an anomalously thin lithosphere.

While xenolith petrology (Pearson et al., 2021) has provided essential information about the composition and history of the continental lithosphere, the principal constraints on lithospheric structure and thickness come from seismology (Artemieva, 2011). Surface-wave tomography (Huang et al., 2003; Priestley et al., 2006; Shen et al., 2016) has provided the primary observation that the mantle lithosphere remains in place beneath Tibet, but it also reveals significant internal structure: slower velocities at around 100 km depth, above faster velocities at around 200 km. If temperature is the primary determinant of shear wave velocity (Priestley and McKenzie, 2013), this stratification is essentially consistent with the laterally averaged structure shown in Fig. 6 produced by overturn of the mantle lithosphere layer. Surface-wave tomographic models are constrained by the apparent propagation speed of dispersed wave-trains that comprise a range of periods. With increasing period, the eigenfunctions for Rayleigh wave propagation are more sensitive to structure at increasing depth, e.g. at 50 s period the phase velocity measurement is most sensitive to shear-wave velocity V_s at depths in the range of about 30-120 km while at 200 s period the sensitivity peaks at depths in the range of about 200-500 km (Ritzwoller and Levshin, 1998). Also increasing with period, the wavelength of 50 s (or 200 s) horizontally propagating Rayleigh waves is around 200 (or 800) km respectively, and hence the ability to resolve the kind of short wavelength lateral variation illustrated in Fig. 4 for the depth range 80-240 km is severely compromised, even if the path sampling is dense. Nonetheless, it is entirely plausible that the depth-variation of the horizontally averaged V_s structure within Tibet is well-resolved, and the observed structure appears consistent with that produced by the overturn of a gravitationally unstable mantle lithosphere. For upper mantle compositions, depletion has little impact on seismic velocity; the principal variations of velocity are determined by temperature (Schutt and Lesher, 2006). Thus a shear-wave velocity profile through the Tibetan upper mantle should detect the modelled inversion of temperatures within a depleted layer which has overturned if the compositional density contrast between the layers is sufficient to preserve the separation of mantle lithosphere from asthenosphere. Vertical sections by both Huang et al. (2003) and Priestley et al. (2006) indeed show the relatively low velocities below the crust, above a higher-velocity layer at depths between 150 and 200 km, before velocity again decreases in the asthenosphere.

While large lateral variations of depth to the LAB are expected when the compositional and thermal density contrasts are comparable (Fig. 4b,5b) it seems unlikely that these variations could be measured seismologically. However, the relatively narrow hot and cold vertical structures that cross the mantle lithosphere present a more feasible target for the technique of teleseismic body-wave tomography. Near-vertically propagating body waves, in principle, can provide the lateral resolution required to identify the velocity signature of these vertical structures given a sufficiently dense and broad-aperture seismic array, even if the technique is relatively insensitive to the depth variations of velocity revealed by the surface-wave studies. The temperature contrast between the hot and cold vertical structures in these calculations is similar to the temperature contrast between a subducted slab and ambient mantle, so the colder material is expected to have a P-wave velocity up to 4% greater than the hot material at the same pressure (Mao et al., 2015). For near vertically propagating P waves that pass through 100 km of the contrasting hot and cold structures we may see up to about 0.5 s difference in relative arrival time, allowing that lateral variations in Moho depth, crustal structure and topography on the LAB interface may complicate analysis.

Ren and Shen (2008) used finite frequency teleseismic tomography to derive images of the lateral variation of lithospheric structure in South-east Tibet, which show (at depths of 112 and 188 km) a remarkable pattern of alternating fast and slow regions. This pattern is vertically continuous, has a characteristic wavelength of 250-300 km and has an interpreted velocity contrast of about 1.5% between fast and slow regions. These strong lateral variations in V_p and V_s could be interpreted as revealing the loci of upwelling and downwelling within a destabilised mantle lithosphere layer. Moreover, Ren and Shen (2008) infer that the measured V_p/V_s ratios in the fast anomalies imply a highly melt-depleted mantle composition. More recently, Qu et al. (2020) reveal a similarly complex pattern of P-wave velocity variation across most of the Tibetan Plateau within the upper 200 km. Full-wave $\mathrm{P_n}$ tomography has also been applied by Bao and Shen (2018) to reveal structures in the upper mantle beneath eastern Tibet, which they associate with convective thinning or delamination processes.

Taken together, the surface wave models that show a laterally averaged stratification, and the teleseismic and full wave $\mathrm{P_n}$ tomography that shows relatively short-wavelength fast and slow regions within the mantle lithosphere, are consistent with the type of gravitational instability depicted in Figs. 4-5b,c. Both types of observation can be explained as the result of an overturn of the mantle lithosphere layer that has remained more or less in place beneath the Tibetan Plateau, constrained by its overall compositional buoyancy. Further analyses of the seismic signature of the Tibetan mantle lithosphere, including more extensive and better-resolved teleseismic body-wave tomography surveys, are needed to determine whether the structures imaged beneath the Tibetan plateau are actually diagnostic of the overturn of an unstable mantle lithosphere layer.

The hypothesised overturn of a relatively buoyant mantle lithosphere layer has a profound and relatively rapid effect on the subsequent thermal evolution of crust and mantle. As illustrated in Figs. 4 and 5, the overturn of the layer causes hot material from the base of the layer to be brought rapidly to near-Moho depths, separated from the crust only by a much thinned remnant of the colder material that was originally the uppermost layer of the mantle lithosphere. Conversely, the colder material is now ponded above the LAB. Although there is a very high degree of lateral variability in the geothermal state of the layer, Fig. 6 shows that the laterally averaged state is well-represented as a simple overturn of the original density profile in the depth range of the mantle lithosphere. Within the mantle lithosphere layer, both density and viscosity serve as proxies of temperature, as shown in Fig. 2, and we can consider the subsequent impact of thermal diffusion on the overturned state, by solving the one-dimensional thermal diffusion equation (details in Appendix) to examine how the average geotherm evolves following the overturn.

Figure 9 shows the evolution of that idealised average geotherm in the first 16 Myr following the initial perturbed state that represents the post-overturn layer. Assuming a constant LAB temperature of 1350°C, heat flows into the base of the layer from the asthenosphere. Similarly, heat flows into the base of the crust (initially at 650°C) from the uppermost mantle lithosphere. The heat flowing into the mantle lithosphere causes a net increase in the average temperature of the whole lithosphere, because it takes much longer for heat to exit the system through the Earth's surface. In this case the thermal content peaks at about 40 Myr before gradually decaying back to the pre-overturn geotherm on a time-scale of about 500 Myr. The increase in mean temperature of the whole lithosphere causes thermal expansion and, under isostatic conditions, the surface elevation of the region rises by about 600 m, most of which occurs in the first 10 Myr following overturn (details in Appendix).

The increase in surface elevation causes an increase in gravitational potential energy that would promote east-west extension in southern Tibet. The link between lithospheric heating and extension in Tibet was originally proposed by England and Houseman (1989) as evidence of a convective thinning event that removed a large fraction of the mantle lithosphere. Although oxygen isotope measurements of basin sediments from Central Tibet (Rowley and Currie, 2006) appear inconsistent with the uplift estimates of England and Houseman (1989), they are not inconsistent (Molnar et al., 2006) with the 600 m estimate obtained here for layer overturn rather than removal. An average increase of 600 m in elevation of the plateau increases the vertical stress component through the upper 160 km of the column of lithosphere by about 20 MPa, causing an increase in the gravitational potential energy (GPE) of order 3 x 10^{12} Nm^{-1}. This change in GPE is relatively large compared to the present force per unit length acting on the Himalayan boundary (estimated at about 8 x 10^{12} Nm^{-1} by Molnar et al., 1993), and thus provides a plausible explanation of why the plateau which developed in a north-south convergent setting switched to east-west extension in the mid-Miocene (England and Houseman, 1989).

The evolution of the average geotherm following overturn of the layer in the simplified model shows that average temperatures at the base of the crust could rise from the initial 650°C to about 900°C within the first 5 Myr or so and would be sustained at that level for about 20 Myr before slowly falling again. One might therefore expect a pulse of felsic magmatism and plutonism with melt generated in the lower crust following the convective overturn of the mantle lithosphere (Platt and England, 1994). The evidence that Tibetan crust has been extensively affected by plutonism is provided by measurements of high seismic wave attenuation and zones of high electrical conductivity in the crust, as summarized by Klemperer (2006). Moreover, the possible mechanical effects of upper mantle overturn on the base of the crust, as seen in the displacement of strain markers and isotherms of Figs. 4 and 5, suggest that plutonic activity within the crust should be correlated with the distribution of upwelling and downwelling in the overturning layer beneath, as suggested by Molnar (2014).

Pulses of alkaline volcanism require a somewhat different mechanism, but an explanation is seen in the likely minor entrainment of asthenospheric melt in the middle of the upwelling regions of the overturning mantle lithosphere layer (Figs. 4 and 5). Such material is fairly rapidly propelled to near sub-crustal depths; the maximum upward velocity in the $a = -1$ case of Figs. 4 and 5 scales to about 20 km/Myr, without considering any additional buoyancy that may be generated by melting. In this environment, entrained material is likely to undergo decompression melting as it approaches the crustal interface, possibly mixing with metasomatised mantle in that layer to give the characteristic high-K signature of Tibetan basalts (Turner et al., 1996; Chung et al., 2005; Ding et al., 2003).

Simple models of a structure the size of the Tibetan Plateau are only plausible when one puts aside the multitude of details that are known from surface observations and geophysical measurements, but we acknowledge the many contributions of thousands of geologists and geophysicists whose observations can be used to test the validity of any model. Reviews like those of (Yin and Harrison, 2000; Yin, 2006; Klemperer, 2006; Kapp and DeCelles, 2019) help us to see the themes below the detail and we acknowledge here the encyclopedic grasp of Tibetan geology by An Yin. His recent passing and those of other major figures like Peter Molnar, and Paul Tapponnier, represent a major loss to the community, but we celebrate their huge contributions to our understanding of the Tibetan Plateau.

Conclusions

The geological evolution of Tibet in the past ~50 Myr is dominated by magmatism, crustal thickening and deformation which has affected the entire region. The activation of normal faulting in Tibet since about 10-15 Ma is one indication that a rapid and significant change in the stress state of the Tibetan lithosphere occurred at about that time. The widely accepted idea that a Rayleigh-Taylor type instability caused dense viscous mantle lithosphere to sink through the upper mantle and be replaced by asthenosphere has been disputed because seismic velocity measurements show fast, cold material at depths of 200 km or more beneath much of the plateau. Instead, we show here that an internal convective overturn of a relatively buoyant Tibetan mantle lithosphere can explain both the seismic shear wave velocity distribution and a recent rapid evolution of the thermal, magmatic and tectonic state of the Tibetan lithosphere. The models described here point to the need for further detailed teleseismic body-wave tomography of the entire Tibetan plateau and the need for further modelling of how asthenospheric material can be entrained and rapidly transported through the mantle lithosphere to produce basaltic melts that reach the surface.

Acknowledgments

This paper has been in development for too many years, but it has benefited very much from discussions with various people including Peter Molnar, Simon Turner, Tim Stern, and Kevin Burke whose comment along the lines of “why do you call this layer lithosphere ?” is entirely apt. We thank Editor A. Zuza, reviewer O. Göğüş, and one anonymous reviewer for constructive comments. The *basil* software library used for the viscous flow calculations is available at: https://github.com/greg-houseman/basil

Appendix: Thermal evolution calculation

The one-dimensional thermal diffusion process is governed by

$$\frac{\partial T}{\partial t} = \kappa \frac{\partial^2 T}{\partial z^2} + H \qquad \text{(A1)}$$

where T is temperature, z is depth, t is time, κ is the thermal diffusivity and H represents a rate of heating caused by radioactive decay, assumed constant in the crustal layer and assumed zero in the mantle lithosphere. The equilibrium solution to this equation $T_{\mathrm{eq}}(z)$ is the quadratic equation represented in Fig. 2 assuming temperature at the Moho ($z = h$) of T_{M} and temperature at the base of the lithosphere ($z = h+L$) of T_{L}. The general solution to the time-dependent problem is represented using a Fourier series:

$$T = T_{eq}(z) + \sum_{n=1}^{\infty} A_n \sin(\frac{n\pi z}{L+h}) \exp(\frac{-\kappa n^2 \pi^2}{(L+h)^2} t) \qquad \text{(A2)}$$

and the coefficients A_n are evaluated using:

$$A_n = \frac{2}{L+h} \int_{z=0}^{L+h} (T_0 - T_{eq}) \sin(\frac{n\pi z}{L+h}) dz \qquad \text{(A3)}$$

where T_0 is the immediate post-overturn profile represented in Fig. 9. As the form of the initial thermal transient is simple, the A_n coefficients can be evaluated analytically:

$$A_n = \frac{2(T_L - T_M)}{n\pi} [-1 - \cos(\frac{Ln\pi}{L+h}) + 2(\frac{L+h}{Ln\pi}) \sin(\frac{Ln\pi}{L+h})] \qquad \text{(A4)}$$

To calculate the effect on surface uplift, the depth integral of density at time t, relative to that at time zero is:

$$\int_0^{L+h} \rho\alpha(T_0 - T(t)) dz = \int_0^{L+h} \rho\alpha \sum_{n=1}^{\infty} A_n \sin\left(\frac{n\pi z}{L+h}\right) \left[1 - \exp\left(\frac{-\kappa n^2 \pi^2}{(L+h)^2} t\right)\right] dz \qquad \text{(A5)}$$

which evaluates as:

$$\int_0^{L+h} \rho\alpha(T_0 - T(t)) dz = 2\rho_m \alpha (L+h) \sum_{n=0}^{\infty} (\frac{A_{2n+1}}{(2n+1)\pi}) [1 - \exp(\frac{-\kappa(2n+1)^2 \pi^2}{(L+h)^2} t)] \qquad \text{(A6)}$$

Following the logic of McKenzie (1978), the changing density in the column produces a change, Δe, in surface level (relative to that at time zero):

$$\Delta e = -\frac{2\rho_m \alpha (L+h)}{\rho_c} \sum_{n=0}^{\infty} \left(\frac{A_{2n+1}}{\pi(2n+1)}\right) \left[1 - \exp\left(\frac{-\kappa(2n+1)^2 \pi^2}{(L+h)^2} t\right)\right] \tag{A7}$$

For Fig. 9, we used L = 160 km, h = 80 km, $\kappa = 10^{-6}$ $m^2 s^{-1}$, ρ_c = 2700 kg m^{-3}, and $\alpha = 3.5 \times 10^{-5}$ K^{-1}.

References

Argand, E., 1924. La tectonique de l' Asie. *Proc. 13th Int. Geol. Cong.*, vol. 7, pp. 171 – 372.

Andersen, J., O.H. Göğüş, R.N. Pysklywec, T. Santimano, and E. Şengül Uluocak, 2022. Symptomatic lithospheric drips triggering fast topographic rise and crustal deformation in the Central Andes, Communications Earth & Environment, 3, 150. ttps://doi.org/10.1038/s43247-022-00470-1

Armijo, R., P. Tapponnier, J. L. Mercier, and H. Tong-Lin, 1986. Quaternary extension in southern Tibet: Field observations and tectonic implications, *J. Geophys. Res.*, 91, 13,803-13,872.

Artemieva, I. M., 2011. *The Lithosphere: An Interdisciplinary Approach*, Cambridge Univ. Press.

Artemieva, I.A. and W.D. Mooney, 2001. Thermal thickness and evolution of Precambrian lithosphere: A global study, *J. Geophys. Res*. 106, 16,387-16,414.

Bao X. and Y. Shen, 2020. Early-stage lithospheric foundering beneath the eastern Tibetan Plateau revealed by full-wave Pn tomography. *Geophys. Res. Lett*., 47, e2019GL086469, doi:10.1029/2019GL086469v

Bird, P., 1979. Continental delamination and the Colorado Plateau, *J. Geophys. Res*., 84, 7561-7571.

Bouhifd, M.A, D. Andrault, G. Fiquet, and P. Richet, 1996. Thermal expansion of forsterite up to the melting point, *Geophys. Res. Lett.*, 23, 1143-1146.

Burchfiel, B.C., L.H. Royden, R.D. van der Hilst, B.H. Hager, Z. Chen, R.W. King, C. Li, J. Lü , H. Yao and E. Kirby, 2008. A geological and geophysical context for the Wenchuan earthquake of 12 May 2008, Sichuan, People's Republic of China, *GSA Today*, v. 18, no. 7, doi:10.1130/GSATG18A.1

Chung, S., M. Chu, Y. Zhang, Y. Xie, C. Lo, T. Lee, C. Lan, X. Li, Q. Zhang and Y. Wang, 2005. Tibetan tectonic evolution inferred from spatial and temporal variations in post-collisional magmatism, *Earth-Science Reviews,* 68, 173 – 196. doi:10.1016/j.earscirev.2004.05.001

Conrad, C.P. and P. Molnar, 1997. The growth of Rayleigh-Taylor-type instabilities in the lithosphere for various rheological and density structures, *Geophys. J. Int.*, 129, 95-112.

Dando, B.D.E, G.W. Stuart, G.A. Houseman, E. Hegedus, E. Bruckl and S. Radovanovic, 2011. Teleseismic tomography of the mantle in the Carpathian-Pannonian region of central Europe, *Geophys. J. Int.*, **186**, 11-31. doi: 10.1111/j.1365-246X.2011.04998.x

Ding, L., P. Kapp, D. Zhong and W. Deng, 2003. Cenozoic Volcanism in Tibet: Evidence for Transition from Oceanic to Continental Subduction, *J. Petrology*, 44, 1833-1865. 10.1093/petrology/egg061

England, P. and G. Houseman, 1989. Extension During Continental Convergence, with Application to the Tibetan Plateau, *J. Geophys. Res*., 94, B12, 17,561-17,579.

England, P., and P. Molnar, 2005. Late Quaternary to decadal velocity fields in Asia, *J. Geophys. Res*., 110, B12401, doi:10.1029/2004JB003541

Fang, J., G.A. Houseman, T.J. Wright, L.A. Evans, T.J. Craig, J.R. Elliott and A. Hooper,The Dynamics of the India-Eurasia Collision: Faulted Viscous Continuum Models Constrained by High-Resolution Sentinel-1 InSAR and GNSS Velocities, *J. Geophys. Res.: Solid Earth*, 129, doi:10.1029/2023JB028571

Gan, W., P. Molnar, P. Zhang, G. Xiao, S. Liang, and K. Zhang, Z. Li, K. Xu, and L. Zhang, 2021. Initiation of Clockwise Rotation and Eastward Transport of Southeastern Tibet Inferred from Deflected Fault Traces and GPS Observations, *Geology*, https://doi.org/10.1130/B36069.1

Gao, S., R.L. Rudnick, R.W. Carlson, W.F. McDonough, and Y.S. Liu, 2002. Re-Os evidence for replacement of the original mantle lithosphere beneath the North China craton. *Earth Planet. Sci. Lett.* 198, 307–322 (2002).

Gao, R., H. Wang, A. Yin, S. Dong, Z. Kuang, A.V. Zuza, W. Li, and X. Xiong, 2013. Tectonic development of the northeastern Tibetan Plateau as constrained by high-resolution deep seismic reflection data, *Lithosphere*, 5, no. 6, p555–574.

Ge, W.-P., P. Molnar, Z.-K. Shen, and Q. Li, 2015. Present-day crustal thinning in the southern and northern Tibetan Plateau revealed by GPS measurements, *Geophys. Res. Lett*., 42, 5227–5235, doi:10.1002/2015GL064347.

Garzanti, E., 2008. Comment on "When and where did India and Asia collide?" by Jonathan C. Aitchison, Jason R. Ali, and Aileen M. Davis, *J. Geophys. Res*., 113, B04411, doi:10.1029/2007JB005276

Garzione, C.N., P. Molnar, J.C. Libarkin, and B.J. MacFadden, 2006. Rapid late Miocene rise of the Bolivian Altiplano: Evidence for removal of mantle lithosphere, *Earth and Planetary Science Letters*, 241(3–4), 543–556. https://doi.org/10.1016/j.epsl.2005.11.026

Göğüş, O.H., R.N Pysklywec, A.M.C. Şengör and E. Gün, 2017. Drip tectonics and the enigmatic uplift of the Central Anatolian Plateau, *Nature Communications*, 8, 1538, doi:10.1038/s41467-017-01611-3

Griffin, W.L., S.Y. O'Reilly, J. C. Afonso and G. C. Begg, 2009. The Composition and Evolution of Lithospheric Mantle: a Re-evaluation and its Tectonic Implications, *J. Petrology*, 50, 1185-1204. doi:10.1093/petrology/egn033

Hatzfeld, D., and P. Molnar, 2010. Comparisons of the kinematics and deep structures of the Zagros and Himalaya and of the Iranian and Tibetan plateaus and geodynamic implications, *Rev. Geophys.*, 48 (2), RG2005, doi:10.1029/2009RG000304

Hirth, G. and D. Kohlstedt, 2013. Rheology of the Upper Mantle and the Mantle Wedge: A

View from the Experimentalists. In: Eiler, J. (Ed.), *Inside the Subduction Factory*, American Geophysical Union. doi:https://doi.org/10.1029/138GM06

Houseman, GA; Barr TD; Evans, LA (2008) Basil: stress and deformation in a viscous material (Ch 3.8, pp77-85) in *Microdynamics Simulation,* ed. Bons, PD.; Koehn, D; Jessell, MW, Lecture Notes in Earth Sciences, **106**, Springer. ISBN: 978-3-540-25522-255

Houseman, G.A., D.P. McKenzie, and P. Molnar, 1981. Convective instability of a thickened boundary layer and its relevance for the thermal evolution of continental convergent belts, *J. Geophys. Res.*, 86, 6115-6132.

Houseman, G.A. and P. Molnar, 1996. Gravitational (Rayleigh-Taylor) instability of a layer with non-linear viscosity and convective thinning of continental lithosphere, *Geophys. J. Int.*, 128, 125-150

Huang, Z., W. Su, Y. Peng, Y. Zheng and H. Li, 2003. Rayleigh-wave tomography of China and adjacent regions, *J. Geophys. Res.*, 108, 2073, doi:10.1029/2001JB001696

Jordan, T.H., 1978. Composition and development of the continental tectosphere, *Nature*, 274, 544-548.

Kapp, P. and P.G. DeCelles, Mesozoic-Cenozoic geological evolution of the Himalayan-Tibetan orogen and working tectonic hypotheses, 2019. *American Journal of Science*, 319, 159 –254, doi:10.2475/03.2019.01

Kaus, B.J.P. and Y.Y. Podladchikov, 2001. Forward and Reverse Modeling of the Three-Dimensional Viscous Rayleigh-Taylor Instability, *Geophys. Res. Lett.*, 28, 1095-1098.

Kay, R.W. and S. Mahlburg-Kay, 1993. Delamination and delamination magmatism. In: A.G. Green, A. Kroner, H.-J. Gotze and N. Pavlenkova (Eds.), Plate Tectonic Signatures in the Continental Lithosphere. *Tectonophysics*, 219, 177-189.

Kind, R., and X. Yuan, 2010. Seismic Images of the Biggest Crash on Earth, *Science*, 329, 1479-1480. doi:10.1126/science.1191620

Klemperer S.L., 2006. Crustal flow in Tibet: geophysical evidence for the physical state of Tibetan lithosphere, and inferred patterns of active flow, *in*: Law, R.D., M.P. Searle and L. Godin,(eds.) Channel Flow, Ductile Extrusion and Exhumation in Continental Collision Zones. *Geological Society, London, Special Publications*, 268, 39–70.

Levander, A., B. Schmandt, M.S. Miller, K. Liu, K.E. Karlstrom, R.S., Crow, C.-T.A. and E.D. Humphreys, 2011. Continuing Colorado Plateau uplift by delamination-style convective lithospheric downwelling. *Nature* **472**, 461–465.

Lorinczi, P., and G.A. Houseman, 2009. Lithospheric gravitational instability beneath the Southeast Carpathians, *Tectonophysics*, **474(1-2)**, pp322-336. doi:10.1016/j.tecto.2008.05.024

Mao, Z., D. Fan, J.F. Lin, J. Yang, S.N. Tkachev, K. Zhuravlev and V.B. Prakapenka, 2015.

Elasticity of single-crystal olivine at high pressures and temperatures, *Earth and Planetary Science Letters,* 426, 204–215.

McDonough, W.F. and S. Sun, 1995. The composition of the Earth, *Chem. Geol.* 120, 223-253.

McKenzie, D.P., 1978. Some remarks on the development of sedimentary basins, *Earth and Planetary Science Letters*, 40, 25-32.

Molnar, P., 2004. Gravitational instability of mantle lithosphere and core complexes, *Tectonics*, 34, 478–487, doi:10.1002/2014TC003808

Molnar, P., P. England, and J. Martinod, 1993. Mantle dynamics, uplift of the Tibetan Plateau and the Indian monsoon, *Reviews of Geophysics*, 31, 357-395.

Molnar, P., G.A. Houseman and P.C. England, 2006. Palaeo-altimetry of Tibet, *Nature*, 444, E4, doi:10.1038/nature05368

Nábelek, J., G. Hetényi, J. Vergne, S. Sapkota, B. Kafle, M. Jiang, H. Su, J. Chen, B. Huang, and the Hi-CLIMB Team, 2009. Underplating in the Himalaya-Tibet Collision Zone Revealed by the Hi-CLIMB Experiment, *Science,* 325, 1371 (2009); doi: 10.1126/science.1167719

Ou, Q., S. Daout, J. R. Weiss, L. Shen, M. Lazecký, T.J. Wright, T. J., and B.E. Parsons, 2022. Large-scale interseismic strain mapping of the NE Tibetan Plateau from Sentinel-1 interferometry, *J. Geophys. Res*. Solid Earth, 127, e2022JB024176. https://doi.org/10.1029/2022JB024176

Pearson, G.D., J.M. Scott, J. Liu, A. Schaeffer, L.H. Wang, J. van Hunen, K. Szilas, T. Chacko and P.B. Kelemen, 2021. Deep continental roots and cratons, *Nature*, 596, 199-211. doi:10.1038/s41586-021-03600-5

Platt J.P., and P.C. England, 1994. Convective removal of lithosphere beneath mountain belts: thermal and mechanical consequences, *Am. J. Sci.*, 294, 307-336.

Poudjom Djomani, Y.H., S.Y. O'Reilly, W.L. Griffin and P. Morgan, 2001. The density structure of subcontinental lithosphere through time, *Earth Planet. Sci. Lett*., 184, 605-621.

Priestley, K., E. Debayle, D. McKenzie, and S. Pilidou, 2006. Upper mantle structure of eastern Asia from multimode surface waveform tomography, *J. Geophys. Res.*, 111, B10304, doi:10.1029/2005JB004082.

Priestley, K. and D. McKenzie, 2013. The relationship between shear wave velocity, temperature, attenuation and viscosity in the shallow part of the mantle, *Earth planet. Sci. Lett.*, 381, 78-91, doi:10.1016/j.epsl.2013.08.022

Qu, C., Y. Xu, W.C. Yang, et al., 2020. P-wave velocity imaging and lithospheric structure of the Tibetan Plateau, *Chinese J. Geophys.* (in Chinese), 63 (3), 847-859, doi:10.6038/cjg2020N0107

Ren, Y., G.W. Stuart, G.A. Houseman, B.D. Dando, C. Ionescu, E. Hegedus, S. Radovanovic, Y. Shen, and SCP Working Group, 2012. Upper mantle structures beneath the Carpathian-

Pannonian region: Implications for the geodynamics of continental collision, *Earth Planet. Sci. Lett..*, **349-350**, 139-152. doi:10.1016/j.epsl.2012.06.037

Ren, Y., and Y. Shen, Finite frequency tomography in south-eastern Tibet: Evidence for the causal relationship between mantle lithosphere delamination and the north–south trending rifts , *J. Geophys. Res.*, 113, B10316, doi:10.1029/2008JB005615

Ritzwoller, M.H. and A.L. Levshin, 1998. Eurasian surface wave tomography: Group velocities, *J. Geophys. Res*., 103, 4839-4878.

Rowley, D.B. and B.S. Currie, 2006. Palaeo-altimetry of the late Eocene to Miocene Lunpola basin, central Tibet, *Nature*, 439, 677–681, doi:10.1038/nature04506

Saleeby, J. and Z. Foster, 2004. Topographic response to mantle lithosphere removal in the southern Sierra Nevada region, California. *Geology* 32, 245–248.

Schutt, D.L. and C.E. Lesher, 2006. Effects of melt depletion on the density and seismic velocity of garnet and spinel lherzolite, J. Geophys. Res., 111, B05401, doi:10.1029/2003JB002950

Shen, W., M. Ritzwoller, D. Kang, Y. Kim, F. Lin, J. Ning, W. Wang, Y. Zheng and L. Zhou, 2016. A seismic reference model for the crust and uppermost mantle beneath China from surface wave dispersion, *Geophys. J. Int*. 206, 954–979. doi: 10.1093/gji/ggw175

Song, X. and S.L. Klemperer, 2024. Numerous Tibetan lower-crustal and upper-mantle earthquakes, detected by Sn/Lg ratios, suggest crustal delamination or drip tectonics, *Earth Planet. Sci. Lett.,* 626,118555.

Stern, T., G.A. Houseman, M. Salmon and L. Evans, 2013. Instability of a lithospheric step beneath western North Island, New Zealand, *Geology*, **41**, pp.423-426. doi: 10.1130/G34028.1

Styron,R.H., M.H. Taylor, K.E. Sundell, D. F. Stockli, J.A.G. Oalmann, A. Möller, A.T. McCallister, D. Liu and L. Ding, 2013. Miocene initiation and acceleration of extension in the South Lunggar rift, western Tibet: Evolution of an active detachment system from structural mapping and (U-Th)/He thermochronology, *Tectonics*, 32, 880–907, doi:10.1002/tect.20053

Tapponnier, P., and P. Molnar, 1977. Active Faulting and Tectonics in China, *J. Geophys. Res.*, 82, 2905-2930.

Turner, S., N. Arnaud, J. Liu, N. Rogers, C. Hawkesworth, N. Harris, S. Kelley, P. Van Calsteren, and W. Deng, 1996. Post-collision, shoshonitic volcanism on the Tibetan Plateau: Implications for convective thinning of the lithosphere and the source of ocean island basalts, *J. Petrol.*, 37, 5-71.

Turner, S., C. J. Hawkesworth, J. Liu, N. Rogers, S. Kelley, and P. van Calsteren, 1993. Timing of Tibetan uplift constrained by analysis of volcanic rocks. *Nature,* 364, 50-53.

Xia, B., I.M. Artemieva, H. Thybo, and S.L. Klemperer, 2023. Strong variability in the thermal structure of Tibetan lithosphere. *Journal of Geophysical Research: Solid Earth*, 128, e2022JB026213. https://doi.org/10.1029/2022JB026213

Yin, A., 2006. Cenozoic tectonic evolution of the Himalayan orogen as constrained by along-strike variation of structural geometry, exhumation history, and foreland sedimentation, *Earth-Science Reviews*, 76, 1 – 131.

Yin, A. and T. M. Harrison, 2000. Geologic evolution of the Himalayan-Tibetan orogen, *Annu. Rev. Earth Planet. Sci.*, 28, 211–80.

Yuan, X., J. Ni, R. Kind, J. Mechie, and E. Sandvol, 1997. Lithospheric and upper mantle structure of southern Tibet from a seismological passive source experiment. *J. Geophys. Res.*, 102, B12, 27491-27500.

Zarunizadeh, Z., K. Motaghi, R. Movaghari, Y. Yang, and K. Priestley, 2024. Seismological constraints on the lithosphere-asthenosphere system beneath the central and east Iranian Plateau, *Tectonophysics,* 873, 230225.

Zhang, Z., Y. Deng, J. Teng, C. Wang, R. Gao, Y. Chen and W. Fan, 2011, An overview of the crustal structure of the Tibetan plateau after 35 years of deep seismic sounding, *J. Asian Earth Sci.*, 40, 977–989.

Figures follow

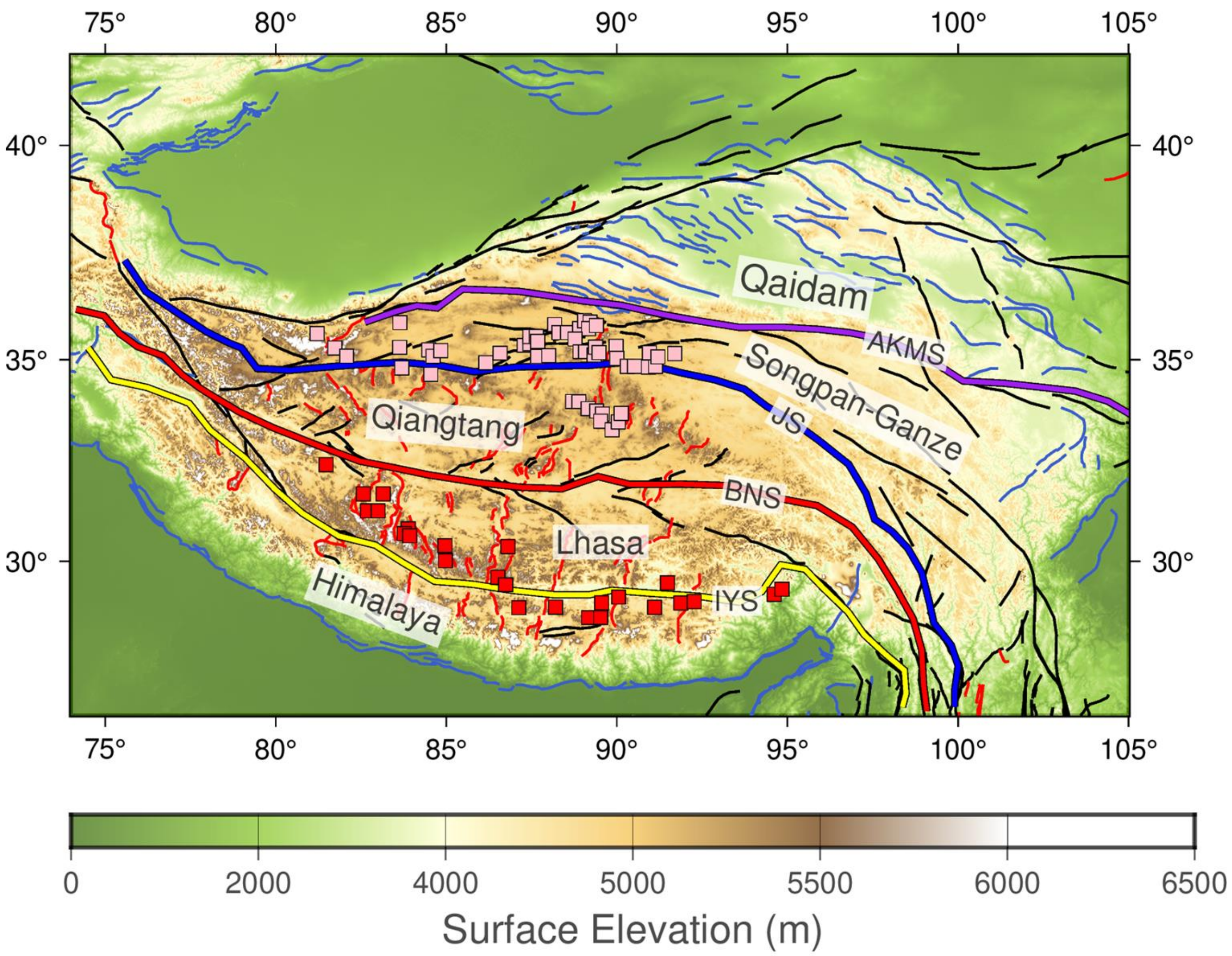

Figure 1. Simplified tectonic and topographic map of the Tibetan Plateau. The major terranes are labelled, separated by sutures resulting from closure of Paleo-Tethys and Neo-Tethys. Abbreviations: AKMS: Anyemaqen suture, JS: Jinsha suture BNS: Bangong–Nujiang suture, IYS: Indus–Yarlung suture. Black/red/blue lines show the locations of active strike-slip/normal/reverse faults from the GEM database https://www.globalquakemodel.org/product/active-faults-database. Squares show locations of Oligocene—Middle-Miocene (pink) and Middle-Miocene—Quaternary (red) volcanism (Chung et al., 2005).

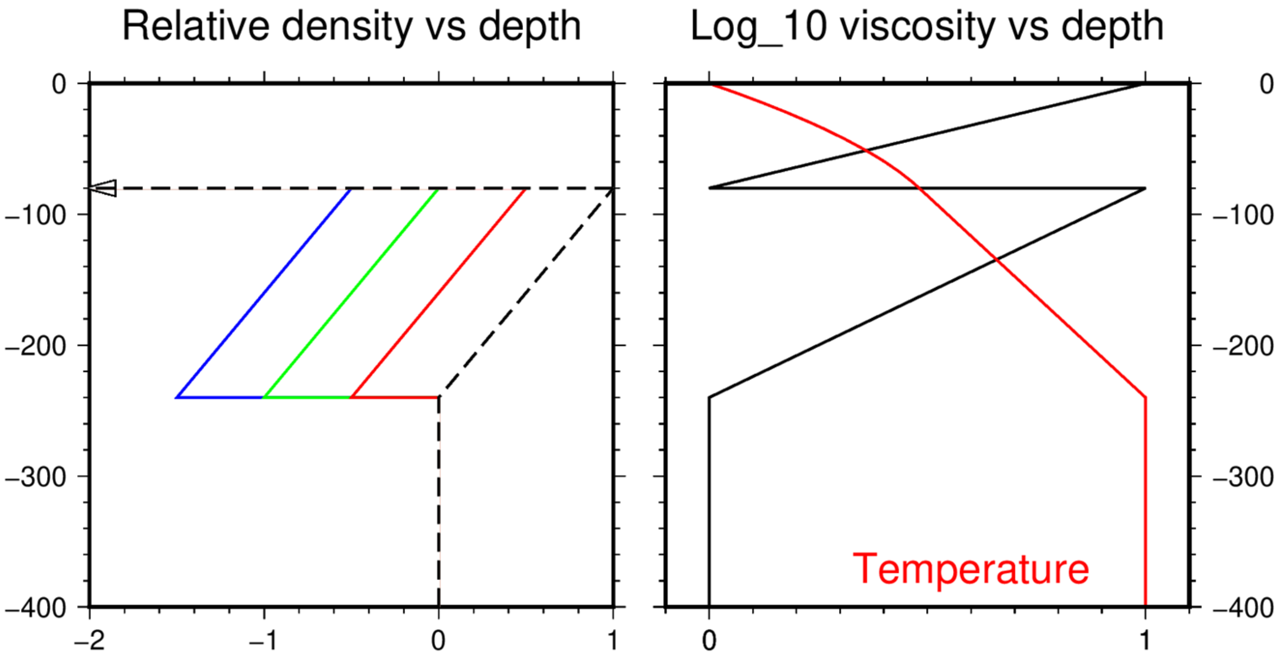

Figure 2. (left) Relative density (dimensionless) vs depth (km) for model cases with a = -0.5 (red), -1 (green), -1.5 (blue), relative to the case in which a = 0 (no intrinsic density contrast; dashed line). The density gradient in the depth range 80-240 km is attributed to thermal expansion dependent on the temperature profile, and the relative density contrast of 1 unit corresponds to about 80 km m^{-3}. (right) Dimensionless temperature (red) and log$_{10}$ of dimensionless viscosity (black) as used in the model calculations shown in the following figures. The assumed thermal profile is based on an equilibrium geotherm for a crustal layer which includes constant radioactive heating sufficient to result in a Moho temperature of 650ºC at 80 km, relative to the assumed LAB temperature of T_a = 1350ºC at 240 km.

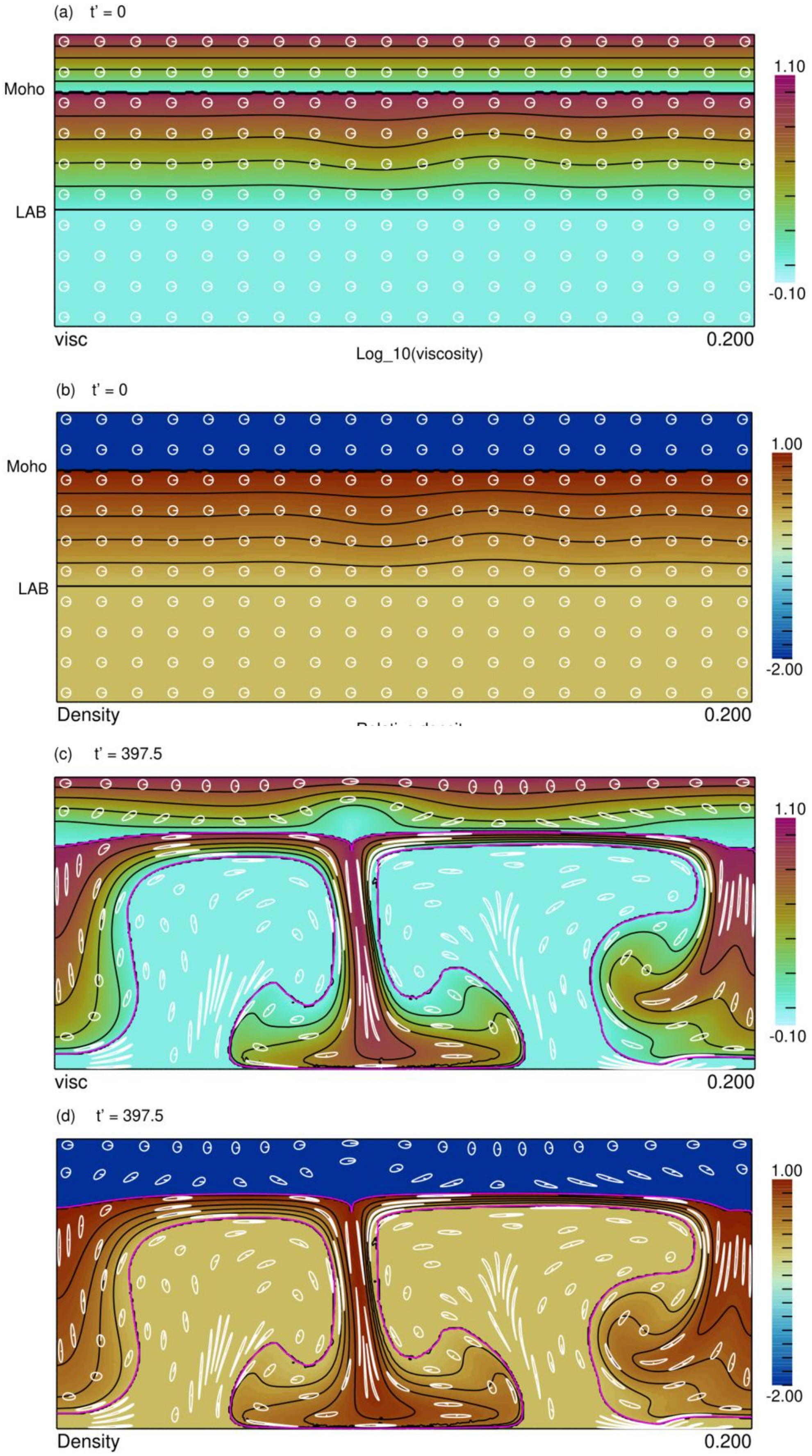

Figure 3. Colour maps show 2D section through idealized model of crust and upper mantle to a nominal total depth of 400 km with no compositional density contrast at the *LAB* for (a) viscosity and (b) relative density, at the initial state *t'* = 0, and (c) viscosity and (d) relative density, for the

evolved instability at $t' = 397.5$ (9.9 Myr for $\eta_0 = 10^{20}$ Pa s). For a,c the colour represents $\log_{10}(\eta/\eta_0)$ with values ranging between 0 ($\eta' = 1$) and 1 ($\eta' = 10$) with an exponential dependence on depth across crust (initially 80 km thick) and mantle lithosphere (initially 160 km thick). For b,d colour represents density relative to asthenosphere, with $\rho' = 0$ in the asthenosphere. Relative density varies between 0 and 1 across the mantle lithosphere and is off-scale in the crust at -7.88. The initially circular markers that are transported and deformed by the mantle flow illustrate the local strain produced by the flow. The magenta contours in c,d mark the major material boundaries (Moho, LAB) that separate mantle lithosphere from crust and asthenosphere.

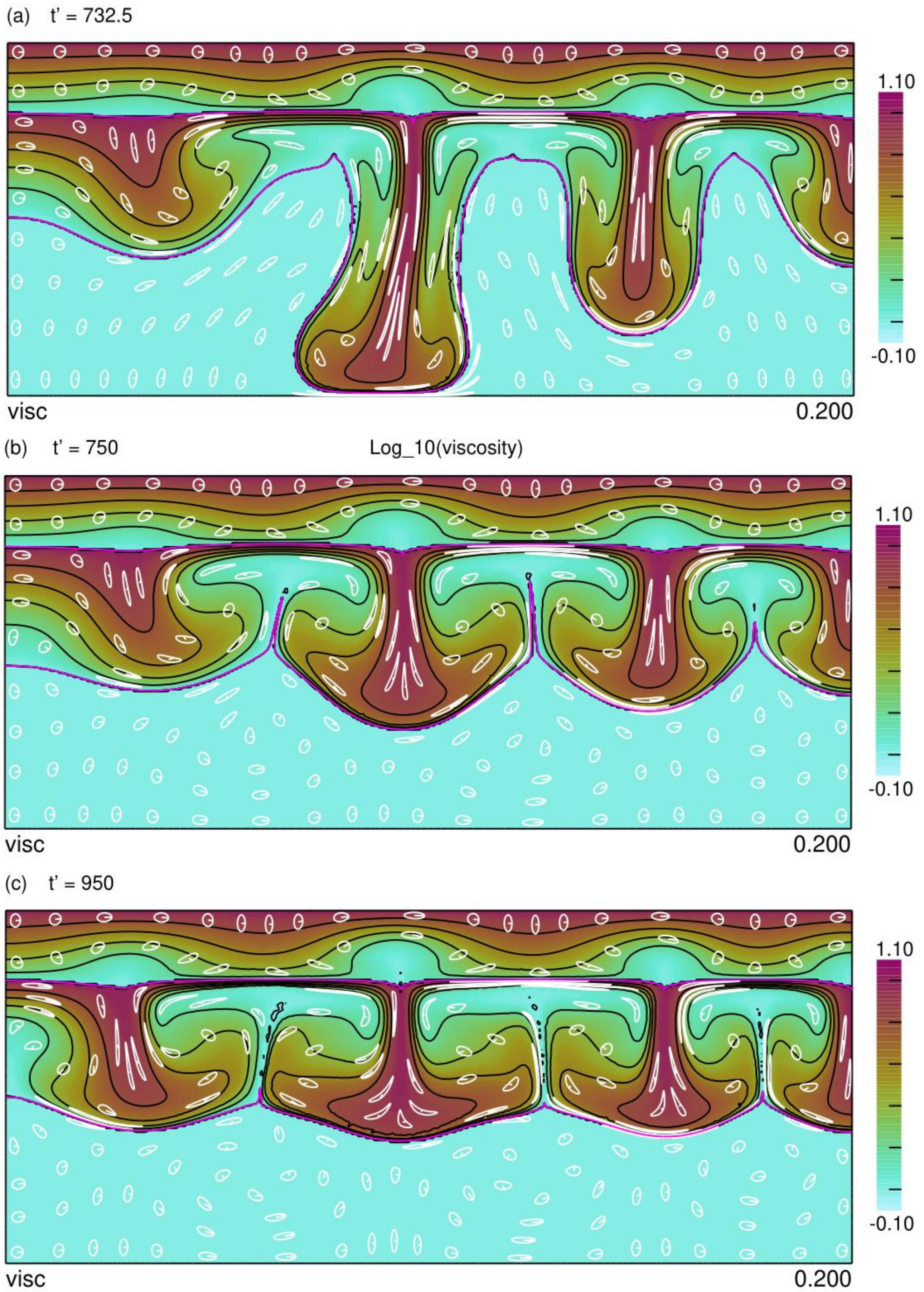

Figure 4. With format as in Fig. 3, these maps show 2D sections of the viscosity after the instability has developed for calculations in which $a = -0.5$, $t' = 732.5$ ($t = 18.3$ Myr) (a), $a = -1$, $t' = 750$ ($t =$

18.8 Myr) (b) and $a = -1.5$, $t' = 950$ ($t = 23.8$ Myr) (c), with dimensional times quoted for $\eta_0 = 10^{20}$ Pa s. In (a) the upper half of the mantle lithosphere is denser than the asthenosphere and is enabled to punch through the asthenosphere. In (b) and (c) the intrinsic buoyancy of the mantle lithosphere is sufficient to contain the circulation within the mantle lithosphere, though in both cases there are large disturbances to LAB topography and upward entrainment of minor amounts of asthenospheric material.

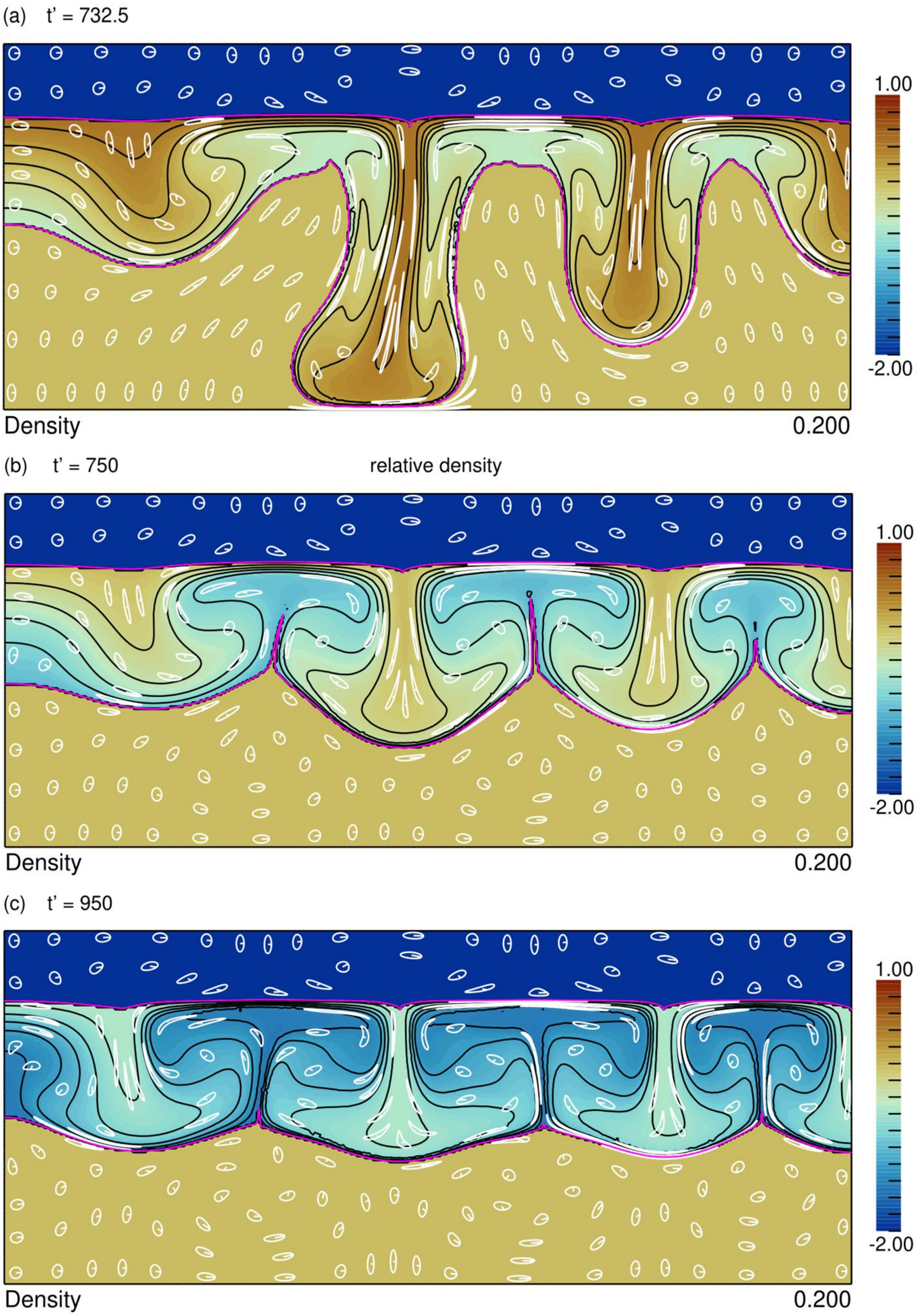

Figure 5. For the same three calculations in Fig. 4, these maps show 2D sections of the relative density variation after development of the instability with $a = -0.5$, $t' = 732.5$ ($t = 18.3$ Myr) (a), $a = -1$, $t' = 750$ ($t = 18.8$ Myr) (b) and $a = -1.5$, $t' = 950$ ($t = 23.8$ Myr) (c), with dimensional times quoted for $\eta_0 = 10^{20}$ Pa s. The reference value ($\rho' = 0$) for the relative density is that of the

asthenosphere, and the relative density within the mantle lithosphere varies from $\rho' = a$ to $1 + a$. The relative density in the crust is off-scale at $\rho' = -7.88$.

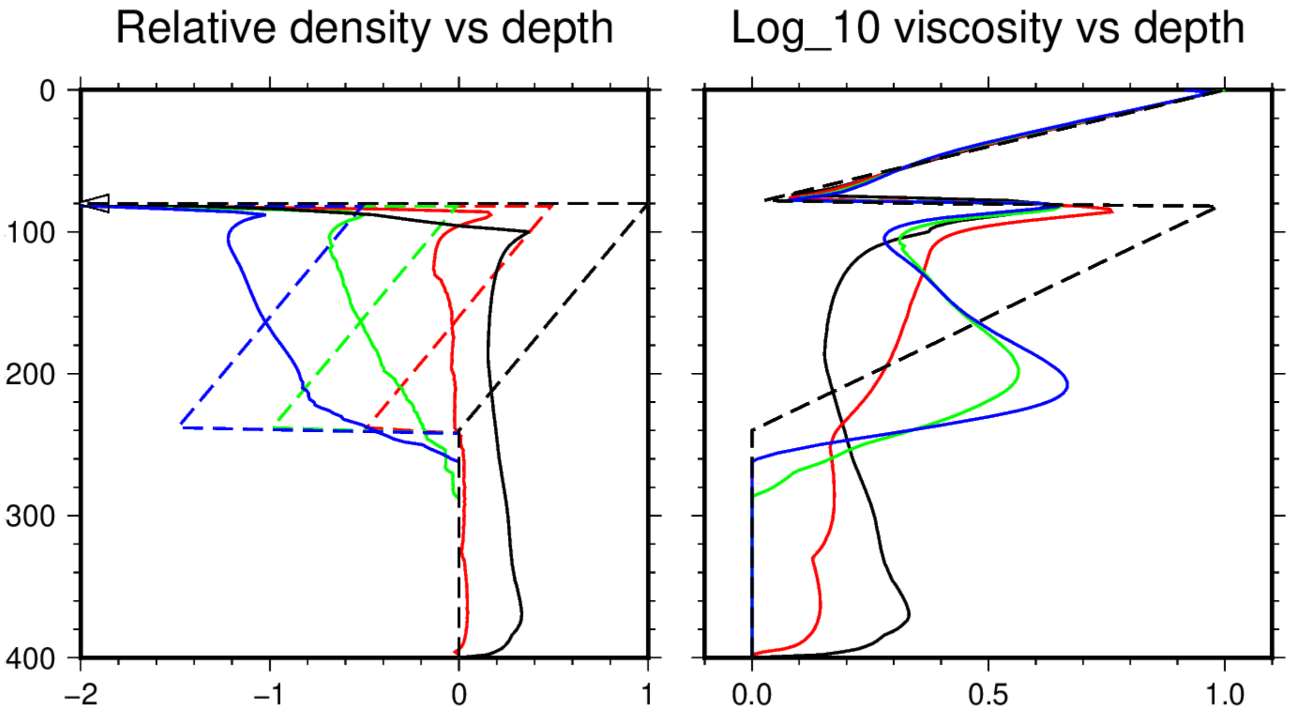

Figure 6. Depth profiles of horizontally averaged relative density (left) and viscosity (right) for the 4 cases illustrated in Figs. 3-5: *a* = 0 (black), *a* = -0.5 (red), -1.0 (green), -1.5 (blue). The dashed lines are those that apply at *t'* = 0, the solid lines apply at the same times shown in Figs. 3-5. The viscosity profiles at *t'* = 0 are the same in all cases. A geometric average is shown for viscosity, that is the lateral average of $\log_{10}(\eta')$ as shown in Figs. 3-5.

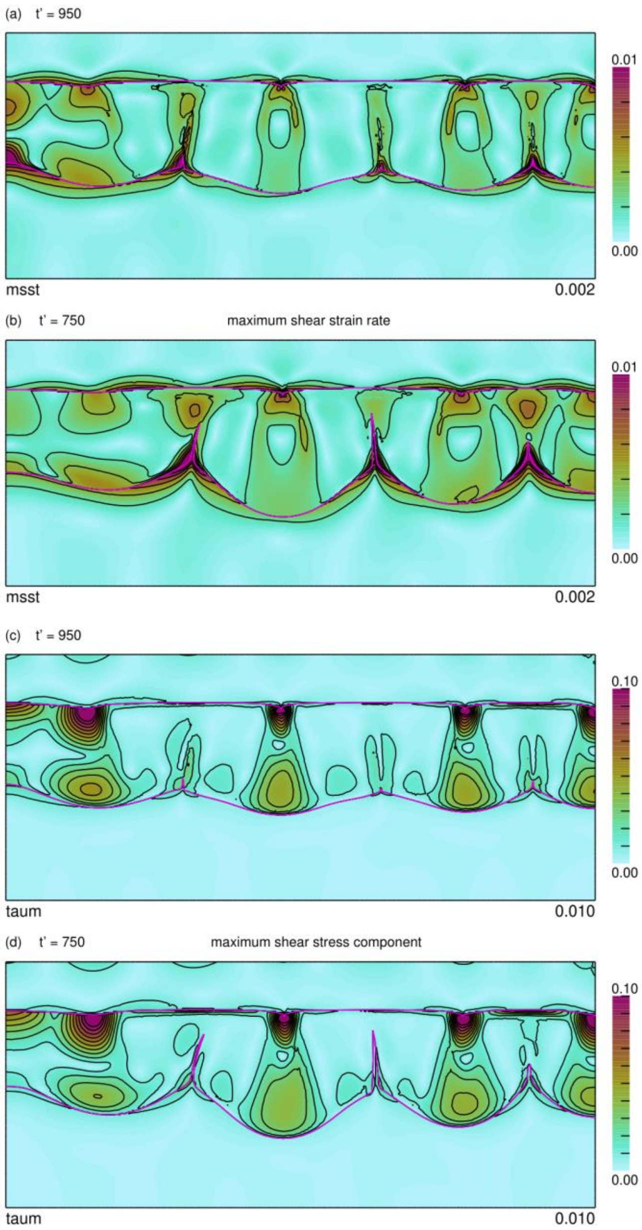

Figure 7. For a = -1.5 (a,c) and a = -1.0 (b,d) at the same times shown in Figs. 4,5 (a) and (b) show contours of the maximum shear strain rate component, (c) and (d) show contours of maximum shear stress component. Contours are labelled in dimensionless units and may be scaled using the scale-factors $gL\Delta\,\rho_T/\eta_0$and $gL\Delta\rho_T$for strain rate and stress respectively (nominally 40.4 per Myr and 128 MPa respectively for $\eta_0 = 10^{20}$ Pa s). The interfaces that represent the model Moho and the model LAB are shown by a magenta line. The colour map is allowed to saturate in places in order to better show some of the second order structure in the solution.

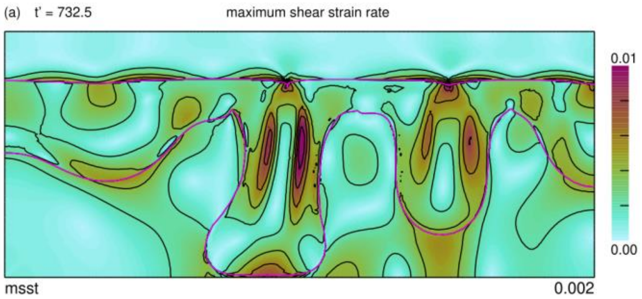

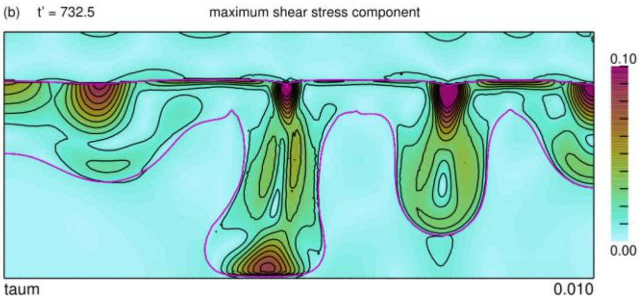

Figure 8. For a = -0.5 at the time as Figs. 4,5a, (a) shows contours of the maximum shear strain rate component, (b) shows contours of maximum shear stress component. Contours are labelled in dimensionless units and may be scaled using the scale-factors $gL\Delta\,\rho_T/\eta_0$ and $gL\Delta\rho_T$ for strain rate and stress respectively (nominally 40.4 per Myr and 128 MPa respectively for $\eta_0 = 10^{20}$ Pa s). The interfaces that represent the original *cr/ml* interface and *ml/as* interface are shown by a magenta line.

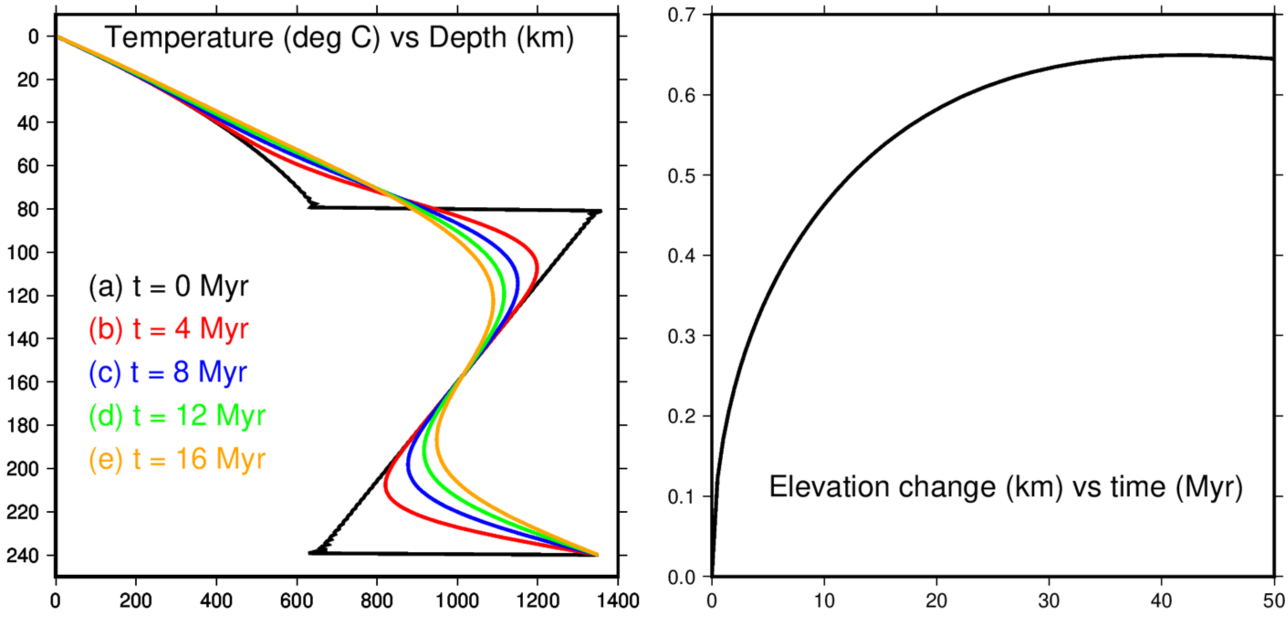

Figure 9. Laterally averaged geothermal profile (left) for the simplified case in which the buoyant mantle lithosphere layer is overturned at time zero (black line) and then re-equilibrates by thermal diffusion. During the re-equilibration heat enters the base of the lithosphere from the asthenosphere beneath and flows into the crust from the top of the lithosphere, so there is a net heating of the layer in the depicted time interval. The net heating causes the upper surface to rise (right) if isostasy prevails. On the time-scale of about 500 Myr the thermal transient decays and the pre-overturn geotherm (Fig. 2) is restored.

Declaration of interests

☒The authors declare that they have no known competing financial interests or personal relationships that could have appeared to influence the work reported in this paper.

☐The authors declare the following financial interests/personal relationships which may be considered as potential competing interests: